

**UNCERTAINTY ANALYSIS ON PHOTOGRAMMETRY-
DERIVED NATIONAL SHORELINE**

BY

FANG YAO

B.S. in Remote Sensing Science and Technology, Wuhan University, 2005

M.S. in Photogrammetry and Remote Sensing, Wuhan University, 2009

THESIS

Submitted to the University of New Hampshire
In Partial Fulfillment of
the Requirements for the Degree of

Master of Science
in
Earth Science
Ocean Mapping

May, 2014

This thesis has been examined and approved.

Thesis Director, Dr. Christopher Parrish
Affiliate Professor, UNH

Dr. Brian Calder
Associate Director, Center for Coastal and Ocean Mapping
Research Associate Professor, UNH

Dr. Shachak Pe'eri
Research Associate Professor, UNH

Dr. Yuri Rzhanov
Research Professor, UNH

Date

ACKNOWLEDGEMENTS

I would like to thank all those people who made this thesis possible.

My first debt of sincere gratitude must go to my advisor, Dr. Christopher Parrish. Given that my previous research background matched his research direction, he accepted me to be his student in the Center for Coastal and Ocean Mapping. For this thesis, he offered his unreserved help and guidance and assisted me with the entire process, from defining the goals and scope of the research to formatting the thesis. I could not have imagined having a better advisor and mentor for my graduate study.

Besides my advisor, I would like to thank the rest of thesis committee: Dr. Brian Calder, Dr. Shachak Pe'eri and Dr. Yuri Rzhanov. They provided valuable and constructive advices to improve my research and thesis. Considering that English is not my first language, they also took efforts to correct my endless writing mistakes. I could not have finished my research and thesis so soon without their encouragement and assistance.

I also thank Center for Coastal and Ocean Mapping. Here I learned a lot of advanced knowledge and technologies. In addition, it provided the funding which allowed me to undertake this research and the opportunity to attend conferences to present my research to others.

Last but not the least, I would like to thank my family: my parents Weixing Yao and Yunhua Tian, my husband Han Hu, and Han's parents Boming Hu and Guilan Yao. They

give me a very carefree environment and unconditional love, so that I can concentrate on my study. I own them too much and wish they could know how much I love and appreciate them. Thanks.

TABLE OF CONTENTS

| | |
|-------------------------|------|
| ACKNOWLEDEgements | iii |
| LIST OF TABLES | ix |
| LIST OF FIGURES | x |
| ABSTRACT | xiii |

| | |
|---|------|
| CHAPTER | PAGE |
| CHAPTER 1 - INTRODUCTION..... | 1 |
| 1.1 Overview of Shoreline | 2 |
| 1.1.1 Definition of Shoreline | 2 |
| 1.1.2 Importance of Shoreline..... | 3 |
| 1.2 Photogrammetric Method for Shoreline Mapping..... | 4 |
| 1.2.1 Shoreline Mapping based on Tide-Coordinated Imagery | 6 |
| 1.2.2 Shoreline Mapping based on Non-Tide-Coordinated Imagery | 10 |
| 1.3 Overview of Uncertainty Modeling..... | 12 |
| 1.3.1 Systematic and Random Uncertainty | 13 |
| 1.3.2 Uncertainty Analysis Methods..... | 13 |

| | |
|--|----|
| 1.3.2.1 Analytical Method | 13 |
| 1.3.2.2 Monte Carlo Method..... | 15 |
| 1.4 Previous Studies for Shoreline Uncertainty Analysis..... | 16 |
| 1.4.1 Field-Survey-Based Method for Photogrammetry-Derived Shoreline Uncertainty..... | 16 |
| 1.4.2 Empirical Method for LiDAR-Derived Shoreline Uncertainty | 17 |
| 1.4.3 Monte Carlo Simulation Method for LiDAR-Derived Shoreline Uncertainty | 18 |
| 1.5 Research Goals | 19 |
| 1.6 Thesis Outline | 19 |
| CHAPTER 2 - STUDY SITE AND STUDY DATA | 21 |
| 2.1 Study Site..... | 21 |
| 2.2 Study Data..... | 23 |
| 2.2.1 Aerial Imagery | 23 |
| 2.2.2 Water Level Data | 24 |
| 2.2.3 Compiled Shorelines | 26 |
| 2.2.4 LiDAR Data | 29 |
| CHAPTER 3 - PHOTOGRAMMETRY-DERIVED SHORELINE UNCERTAINTY ANALYSIS..... | 31 |
| 3.1 Shoreline Uncertainty based on Tide-Coordinated Imagery | 31 |
| 3.1.1 Exterior Orientation Element Uncertainty | 31 |

| | |
|---|----|
| 3.1.2 Offset between MHW or MLLW Datum and Observed Water Level..... | 38 |
| 3.1.3 Uncertainty in Water Level Data | 40 |
| 3.1.4 Human Compilation Uncertainty | 48 |
| 3.1.5 Total Propagated Uncertainty | 51 |
| 3.2 Shoreline Uncertainty based on Non-Tide-Coordinated Imagery | 55 |
| 3.2.1 Exterior Orientation Element Uncertainty | 55 |
| 3.2.2 Uncertainty in Water Level Data | 55 |
| 3.2.3 Human Compilation Uncertainty | 55 |
| 3.2.4 Total Propagated Uncertainty | 56 |
| CHAPTER 4 – EXPERIMENTAL RESULT..... | 58 |
| 4.1 Shoreline Uncertainty based on Tide-Coordinated Imagery | 58 |
| 4.1.1 Exterior Orientation Element Uncertainty | 58 |
| 4.1.2 Offset between MLLW Datum and Observed Water Level | 66 |
| 4.1.3 Uncertainty in Water Level Data | 66 |
| 4.1.4 Human Compilation Uncertainty | 68 |
| 4.1.5 Total Propagated Uncertainty | 69 |
| 4.2 Shoreline Uncertainty based on Non-Tide-Coordinated Imagery | 71 |
| 4.2.1 Exterior Orientation Element Uncertainty | 71 |
| 4.2.2 Uncertainty in Water Level Data | 71 |
| 4.2.3 Human Compilation Uncertainty | 71 |

| | |
|---|----|
| 4.2.4 Total Propagated Uncertainty | 73 |
| CHAPTER 5 – DISCUSSION..... | 76 |
| 5.1 Exterior Orientation Element Uncertainty | 76 |
| 5.2 Tidal Zoning Uncertainty..... | 77 |
| 5.3 Human Compilation Uncertainty | 77 |
| 5.4 Comparison of Tide-Coordinated and Non-Tide-Coordinated Uncertainties | 78 |
| 5.5 Relationship between Uncertainty and Slope | 79 |
| CHAPTER 6 – CONCLUSIONS AND RECOMMENDATIONS FOR FUTURE WORK | |
| | 82 |
| LIST OF REFERENCES | 85 |
| APPENDIX: TIDE ANALYSIS REPORT FOR ME1001..... | 92 |

LIST OF TABLES

| | |
|---|----|
| Table 2.1 Image acquisition parameters | 24 |
| Table 2.2 Tide Analysis Report (provided by NGS) | 25 |
| Table 2.3 Compilation result analysis for 2003 Fort Desoto, Florida project | 27 |
| | |
| Table 3.1 Uncertainty components for tide-coordinated shoreline..... | 53 |
| Table 3.2 Uncertainty components for non-tide-coordinated shoreline | 56 |
| | |
| Table 4.1 The uncertainty of the ground coordinates caused by the exterior orientation element uncertainties | 61 |
| Table 4.2 The exterior orientation elements of the first image pair..... | 62 |
| Table 4.3 The exterior orientation elements of the simulated image pair | 64 |
| Table 4.4 Tidal zoning uncertainty analysis for Coffins Point | 67 |
| Table 4.5 Tide-coordinated human compilation uncertainty computation..... | 68 |
| | |
| Table 5.1 The planimetric values (in meters) of each uncertainty component and the total uncertainties for the survey area | 79 |

LIST OF FIGURES

| | |
|---|----|
| Figure 1.1 Marine boundaries defined by shorelines | 3 |
| Figure 1.2 Shoreline mapping, using a plane table and an alidade | 5 |
| Figure 1.3 MLLW tide windows | 7 |
| Figure 1.4 A digital photogrammetric system | 8 |
| Figure 1.5 Tide-coordinated imagery | 9 |
| Figure 1.6 Non-tide-coordinated imagery..... | 11 |
| Figure 1.7 Cross section drawing which shows the relationship between MHW datum and observed water level | 12 |
| Figure 1.8 Field-survey-based method for assessing the photogrammetry-derived shoreline uncertainty..... | 17 |
| | |
| Figure 2.1 The survey area for ME1001 | 21 |
| Figure 2.2 The tides at Cobscook Bay | 22 |
| Figure 2.3 The mosaic natural color imagery overlaid on NOAA Chart..... | 23 |
| Figure 2.4 The mosaic near infrared imagery | 24 |
| Figure 2.5 MHW and MLLW lines for the survey area | 26 |
| Figure 2.6 Two selected areas for non-tide-coordinated human compilation uncertainty analysis (red boxes)..... | 28 |
| Figure 2.7 Compiled MHW lines from 9 compilers | 29 |
| Figure 2.8 LiDAR data for the ME1001 survey area..... | 30 |

| | |
|--|----|
| Figure 3.1 Space intersection | 34 |
| Figure 3.2 Configuration of the Monte Carlo analysis method for determining positioning uncertainty caused by exterior orientation element uncertainty for each image pair | 38 |
| Figure 3.3 Offset between the observed water level and MLLW datum at the time the image was taken..... | 39 |
| Figure 3.4 An example of Pydro-generated water level relative to MHW and MLLW at the time of acquisition of each image | 40 |
| Figure 3.5 TCARI water level uncertainty | 41 |
| Figure 3.6 The tide gauge design used to reduce the current-induced uncertainty..... | 43 |
| Figure 3.7 Human compilation uncertainty analysis | 50 |
| Figure 3.8 Flowchart of human compilation uncertainty computation..... | 51 |
| | |
| Figure 4.1 The relationships between the number of the simulation trials and X/Y/Z uncertainty caused by exterior orientation element uncertainties..... | 60 |
| Figure 4.2 The influence of the exterior orientation element uncertainties and the photographic scale on the point positioning uncertainty (for the first image pair)..... | 64 |
| Figure 4.3 The influence of the exterior orientation element uncertainties and the photographic scale on the point positioning uncertainty (for the simulated image pair).. | 65 |
| Figure 4.4 Filtered slope raster imagery | 70 |
| Figure 4.5 The reference shorelines (red lines) and transects (blue lines)..... | 72 |
| Figure 4.6 The relationship between the slope and the planimetric human compilation uncertainty..... | 73 |

| | |
|--|----|
| Figure 4.7 The uncertainty boundaries | 74 |
| Figure 5.1 Distribution of standard uncertainties for tide-coordinated and non-tide-coordinated compilation..... | 80 |
| Figure 5.2 Distribution of slopes | 81 |

ABSTRACT

UNCERTAINTY ANALYSIS ON PHOTOGRAMMETRY-DERIVED NATIONAL SHORELINE

by

Fang Yao

University of New Hampshire, May, 2014

Photogrammetric shoreline mapping remains the primary method for mapping the national shoreline used by the National Geodetic Survey (NGS) in the National Oceanic and Atmospheric Administration (NOAA). To date, NGS has not conducted a statistical analysis on the photogrammetry-derived shoreline uncertainty. The aim of this thesis is to develop and test a rigorous total propagated uncertainty (TPU) model for shoreline compiled from both tide-coordinated and non-tide-coordinated aerial imagery using photogrammetric methods. Survey imagery collected over a study site in northeast Maine was used to test the TPU model. The TPU model developed in this thesis can easily be extended to other areas and may facilitate estimation of uncertainty in inundation models and marsh migration models.

CHAPTER 1 - INTRODUCTION

National shoreline products should be accompanied by uncertainty estimates. These uncertainties enable users to evaluate the suitability of the national shoreline for other applications, such as coastal change analysis, and assist in making policy decisions in coastal zone management. Photogrammetric stereo compilation has been the main method for shoreline mapping used by the National Geodetic Survey (NGS) since 1927, but statistical uncertainty analysis has lagged behind other areas of technology development in photogrammetric shoreline compilation. The only uncertainty estimation method for the photogrammetry-derived shoreline that has been well tested and documented to date is a field survey technique based on high-precision Global Positioning System (GPS), which is time consuming and economically expensive. In addition, the fieldwork is difficult to conduct in all shoreline survey regions. Therefore, a statistical model for photogrammetry-derived uncertainty analysis is needed, which not only satisfies international hydrographic surveying standards, but can also provide sensitivity analysis for each uncertainty influence factor.

1.1 Overview of Shoreline

1.1.1 Definition of Shoreline

In many publications, a shoreline is succinctly defined as the line where the water and land meet. However, due to the influence of some factors, such as wave swash, tides, currents, storms, seasonal beach changes, sediment transportation, natural and human-induced sea-level changes, the line of intersection between water and land changes continuously (Graham *et al.*, 2003; Parrish, 2012). Therefore, this succinct definition is not useful in practice (e.g., in mapping applications and coastal change analysis), as it is not meaningful to compare intersection lines from different times that depend on the tidal cycle.

In order to circumvent the above problem, many shoreline indicators have been used in shoreline mapping and described in many publications. However, it is difficult for the practitioners to agree on a common shoreline indicator. All indicators can be divided into two categories: (1) physical shoreline indicators (Stokdon *et al.*, 2002; Boak and Turner, 2005), including berm crest, scarp edge, vegetation line, dune toe, dune crest, and cliff or bluff crest and toe; and (2) water-level based shoreline indicators (Shalowitz, 1964; Pajak and Leatherman, 2000), including the high water line, mean high water (MHW) line, mean lower low water (MLLW) line, wet/dry boundary, wet sand line, and water line, etc.

Currently, NGS, the part of the National Oceanic and Atmospheric Administration (NOAA), which is responsible for mapping the national shoreline depicted on NOAA nautical charts, compiles the MHW line and MLLW line as shoreline indicators in order to minimize the tidal daily, monthly and yearly variations (Office of Coast Survey, 2013a). MHW is the average of all the high water heights observed over the National Tidal Datum

Epoch (NTDE), a specific 19-year period which contains all the tidal periods that need to be considered in tidal computations, whereas MLLW is the average of all the lower low water heights observed over the NTDE. MHW and MLLW lines are typically marked on United States (U.S.) NOAA nautical charts. MHW lines are the legal lines of the U.S. and the boundaries between land and sea. MLLW lines help to define America's territorial limits, the Exclusive Economic Zone, and the High Seas (Woodlard *et al.*, 2003).

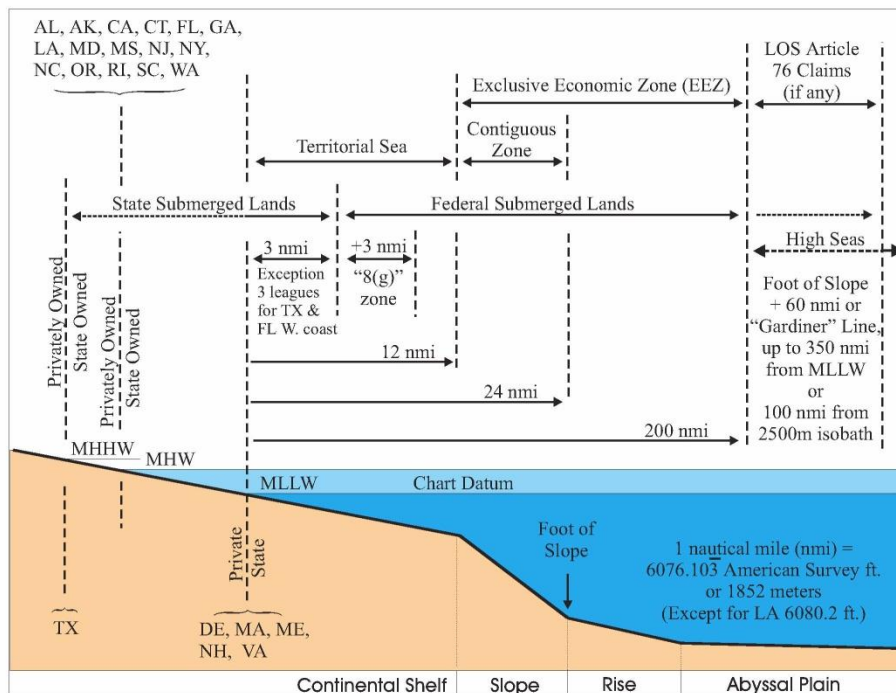


Figure 1.1 Marine boundaries defined by shorelines. (Courtesy of Office of General Counsel, NOAA, 2014)

1.1.2 Importance of Shoreline

The areas around the shoreline are rich with diverse species, habitat types, nutrients and natural resources (WRI, 2000). In addition, approximately half of the world's population lives within 200 kilometers of the shoreline (Creel, 2003), and, in the U.S., about 53% of

the nation's population lives in the 673 U.S. coastal counties (Crossett *et al.*, 2004). Currently, sea level is rising at the rate of ~3 mm/year worldwide (Royal Swedish Academy of Sciences, 2012), and local rates of sea level rise are higher in some regions. Sea-level rise can lead to a loss of coastal land and wetland species, such as fish, bird, wildlife and plants. It can also increase the frequency and extent of coastal flooding, as well as the impact of coastal storms. Therefore, in order to better understand and analyze these impacts mentioned above, mapping shorelines has become a significant task worldwide.

Furthermore, an accurately mapped shoreline is of extreme importance to nautical charting agencies/offices, as well as coastal scientists and coastal zone managers. It supports safe marine navigation, and legal property boundary definition, as well as a wide range of coastal science and resource management applications (shoreline change, sea-level rise, inundation modeling, habitat change, wetlands studies, restoration, etc.) (e.g., Boak and Turner, 2005).

1.2 Photogrammetric Method for Shoreline Mapping

The earliest shoreline survey in the U.S. was conducted by the U.S. Coast Survey in 1834 along the north shore of Great South Bay, Long Island (Wainwright, 1922). The procedures of the historical shoreline surveys were field based (Graham *et al.*, 2003) (Figure 1.2).



Figure 1.2 Shoreline mapping, using a plane table and an alidade (Courtesy of NGS, 2014a)

Shoreline mapping changed from a field survey approach to a remote sensing approach with the advent of the airplane and aerial camera. In 1919, the U.S. investigated the feasibility of aerial photography in shoreline mapping over coastal New Jersey. However, shoreline mapping was still conducted by field surveys until 1927 (Smith, 1981). With the increase use of aerial photogrammetric methods since 1927, aerial survey has been used for mapping shorelines to update nautical charts and is still the primary method for shoreline mapping in NOAA. Compared with field-based shoreline mapping methods, photogrammetric methods have several benefits, including the ability to map large areas with greater detail quickly, and to access certain areas where field surveys cannot be conducted. As aerial imagery evolved from visible panchromatic to multi-spectral bands that include three bands in the visible range (red-green-blue) and one band in the near-infrared range, shoreline mapping procedures using photogrammetry became more

accurate and robust. Compared with black and white imagery (i.e., a panchromatic band in the visible range), color imagery better represents the real world, from which operators can more easily and better identify and interpret features. In the near infrared (NIR) portion of the electromagnetic spectrum, water absorbs nearly all the light, which makes water appear very dark, while land (such as sand and vegetation) has a bright reflectance in this spectral region. The high contrast between land and water makes it easier to interpret and map shorelines in NIR imagery. The transition from film-based imagery to digital format also reduces the time needed from acquisition to a shoreline product.

Currently, photogrammetric shoreline mapping is mainly conducted on tide-coordinated imagery (taken when the vertical difference between water level and MHW or MLLW is within a defined tolerance) and non-tide-coordinated imagery (taken when the vertical difference between water level and MHW or MLLW is out of a defined tolerance).

1.2.1 Shoreline Mapping based on Tide-Coordinated Imagery

Tide-coordinated imagery must be acquired when the tide stage is within the defined tolerance of MHW or MLLW, which is called the tide window (Graham *et al.*, 2003):

$$T_r = \begin{cases} \pm 0.09, & r \leq 1.5m \\ \pm 0.1r, & r > 1.5m \end{cases} \quad (1.1)$$

where T_r is the tolerance in meters, and r is the tide range. Figure 1.3 shows the MLLW tide windows from a water level prediction.

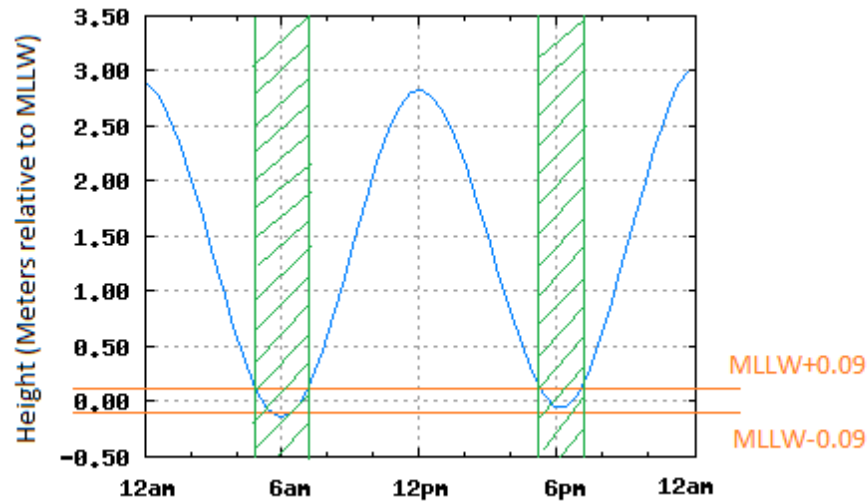


Figure 1.3 MLLW tide windows

The tide window is the constraint on image acquisition time. NOAA specifies additional aerial imagery acquisition requirements for shoreline mapping programs in the “Scope of Work for Shoreline Mapping under the NOAA Coastal Mapping Program” (Leigh *et al.*, 2012) in order to acquire aerial imagery with good quality, on which ground objects and shorelines can be identified and extracted easily.

In shoreline mapping programs, kinematic GPS and Inertial Measurement Unit (IMU) devices are often used to determine positioning and orientation parameters of image exposure stations. In this case, ground control may not be needed, or, at least, can be greatly reduced. This is very useful in areas which cover a lot of water or forest, because ground control points in these areas are difficult to interpret on the imagery.

Feature compilation is performed in a stereo environment of a digital photogrammetric system (Figure 1.4). BAE's SOCET SET is a photogrammetric software program commonly used by NGS to map shorelines (Graham *et al.*, 2003). Three-dimensional coordinates of ground points are estimated by measurements made in stereo image pairs

(adjacent but overlapping aerial images). A ray can be constructed from an exposure station to a ground point, and the three-dimensional coordinates of the ground point are determined by the intersection of the corresponding rays (Mikhail *et al.*, 2001).



Figure 1.4 A digital photogrammetric system, which consists of a desktop computer with specified photogrammetric software, a 3D pointing device and a stereo display system (Courtesy of NOS, 2014)

Ideally, compilers trace the land-water interface as the MHW or MLLW line in NIR tide-coordinated imagery because of the sharp contrast between land and water in NIR. However, wave action may hamper the shoreline interpretation given that it may create swash zones (Graham *et al.*, 2003). In order to minimize the effect of wave action, tide-coordinated shoreline is usually delineated in the middle of the average run-up and retreat limits of the waves. In addition, some indicators can be used to assist shoreline interpretation, such as the tide's falling or rising, beach features, berms, tone and texture. Figure 1.5 shows the MHW and MLLW lines interpreted from tide-coordinated imagery.

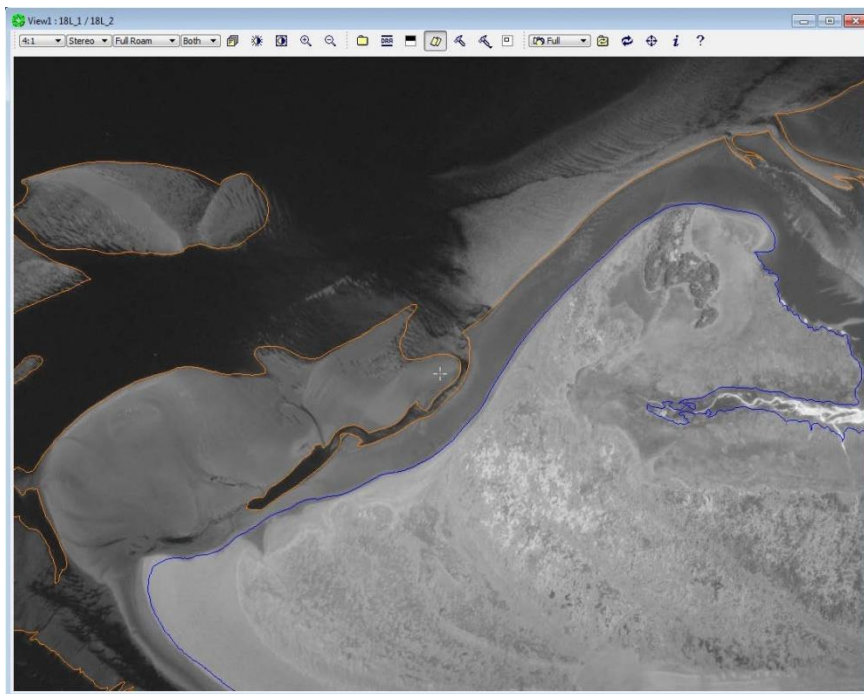
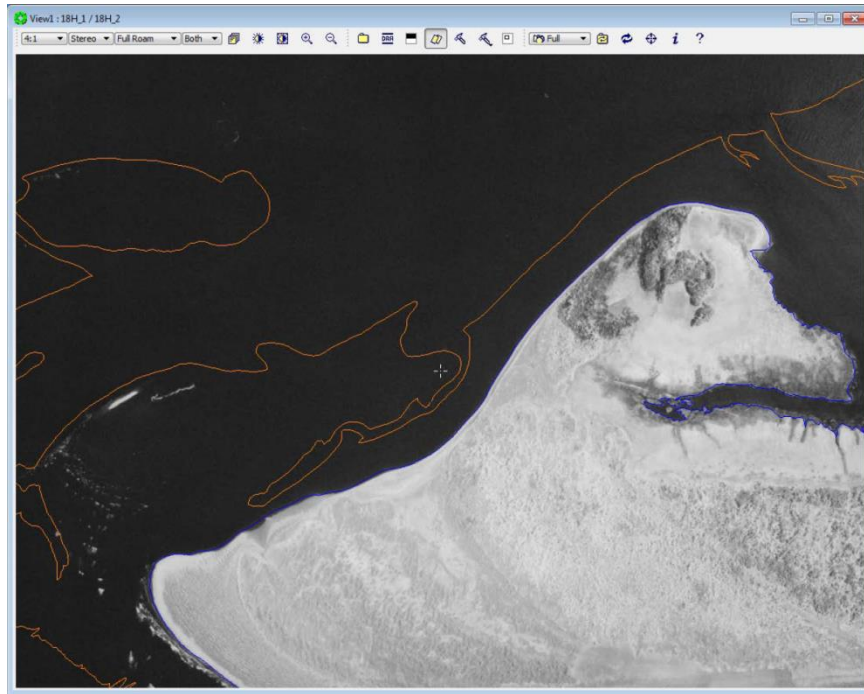


Figure 1.5 Tide-coordinated imagery. (Top) is MHW tide-coordinated imagery, from which the MHW line (the blue line) is interpreted. (Bottom) is MLLW tide-coordinated imagery, from which the MLLW line (the orange line) is interpreted.

1.2.2 Shoreline Mapping based on Non-Tide-Coordinated Imagery

When the water level is out of the defined tolerance and below the MHW datum, compliers will delineate the MHW line mainly based on elevation information on non-tide-coordinated imagery. Natural color imagery is often used as non-tide-coordinated imagery given that it can provide more indicators to assist in shoreline compilation. The MLLW line is seldom compiled on non-tide-coordinated imagery. It is not technologically difficult, but rather there are fewer opportunities to acquire the imagery when water level is below the MLLW datum (White *et al.*, 2011).

The differences between non-tide-coordinated and tide-coordinated shoreline mapping mainly include: (1) the time of imagery acquisition: tide-coordinated imagery is taken within the MHW or MLLW tide window period; non-tide-coordinated imagery is taken when the water level is below the MHW datum; and (2) the compilation method used in the shoreline mapping procedure: for tide-coordinated imagery, the land-water interface is compiled as MHW or MLLW shoreline; for non-tide-coordinated imagery, the MHW shoreline is compiled based on stereoscopic measurement of an elevation contour. Figure 1.6 shows non-tide-coordinated imagery on which the MHW shoreline (the blue line) has been compiled. The MHW shoreline is not the intersection between the water and the land on this imagery.

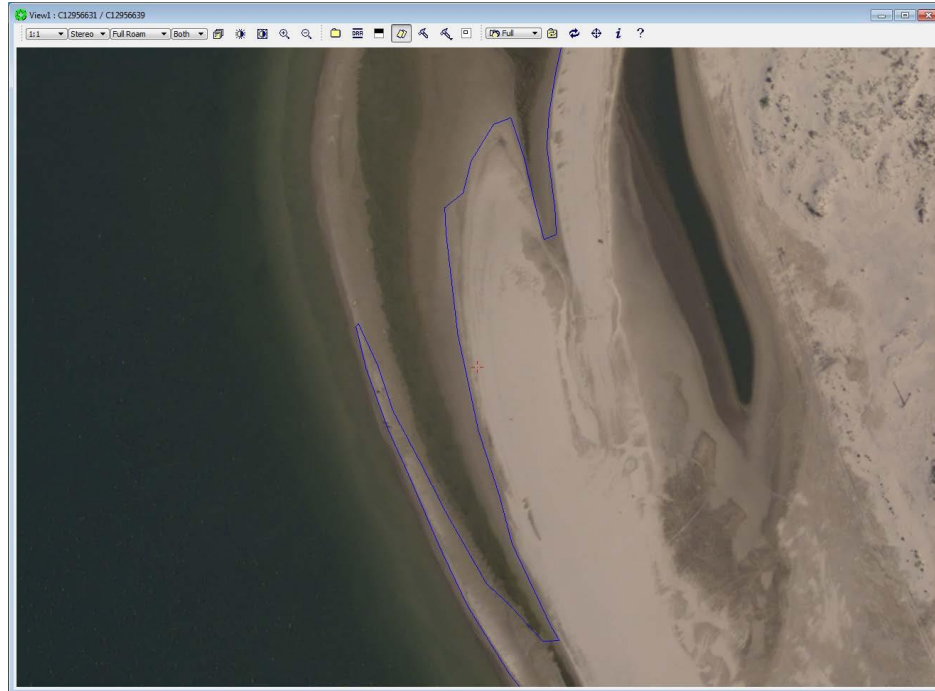


Figure 1.6 Non-tide-coordinated imagery. The blue line is MHW shoreline compiled on the non-tide-coordinated imagery.

The procedure for shoreline mapping from non-tide-coordinated imagery only describes the difference from tide-coordinated shoreline mapping as follows:

- (1) Acquire imagery when the water level is below the MHW datum based on predicted water level data.
- (2) Obtain the vertical offset between the MHW datum and observed water level based on observed water level data.
- (3) Measure the elevation of the ground just landward of the land-water interface.
- (4) Raise the floating mark up by the vertical offset between the MHW datum and observed water level to contour the MHW shoreline (Figure 1.7). (Note: a floating mark is a mark used to indicate the three-dimensional location of a point in a stereo image pair, and it is used by a photogrammetrist in making stereoscopic measurement (Philpot, 2012)).

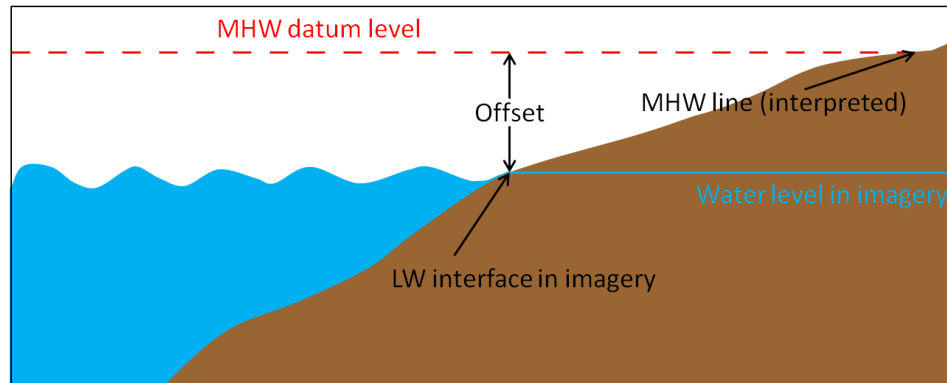


Figure 1.7 Cross section drawing which shows the relationship between MHW datum and observed water level

In addition to photogrammetric shoreline mapping methods, several alternative technologies were investigated by NGS for shoreline mapping. These include: Light Detection And Ranging (LiDAR) (Stockdon *et al.*, 2002; Wozencraft and Millar, 2005; Brock and Purkis, 2009; White *et al.*, 2011), satellite imagery (NGS, 2014b), Interferometric Synthetic Aperture Radar (IFSAR) (NGS, 2014c), Synthetic Aperture Radar (SAR) (Alfugara *et al.*, 2011), and hyperspectral imagery (Graham *et al.*, 2003). In this thesis, the research will only focus on the photogrammetric shoreline mapping methods.

1.3 Overview of Uncertainty Modeling

As the International Hydrographic Organization (IHO) Standards for Hydrographic Surveys (S-44) specifies, the uncertainty should be recorded together with the survey data and meet the IHO requirements. The required positioning uncertainty of the coastline (or shoreline) at the 95% confidence level is defined to be 10 m for special order and 20 m for order 1a, 1b and 2 (IHO, 2008).

1.3.1 Systematic and Random Uncertainty

Measurement uncertainties can be divided into two basic types: systematic uncertainty and random uncertainty. Systematic uncertainty is a consistent difference between the measurements and the actual value of the measured attribute. Random uncertainty is the uncertainty in measurement which leads to the measurement results being inconsistent when measuring a constant attribute or quality many times. The cause of systematic uncertainty can usually be identified, and it can often be estimated and thus eliminated. The random uncertainty cannot be eliminated. We can only reduce it by averaging a large number of measurement results under suitable observing conditions (Dieck, 2002).

1.3.2 Uncertainty Analysis Methods

In this study, two uncertainty analysis methods are investigated: analytical methods and Monte Carlo methods.

1.3.2.1 Analytical Method

If the relationship between a measurand Y and a set of the input quantities $\{X_i, 1 \leq i \leq N\}$ is expressed by

$$Y = f(X_1, X_2, \dots, X_n) \quad (1.2)$$

then an estimate of the measurand Y , denoted by y , can be obtained by the function f using the input estimates x_1, x_2, \dots, x_n for the values of n input quantities X_1, X_2, \dots, X_n ,

$$y = f(x_1, x_2, \dots, x_n) \quad (1.3)$$

The total propagated uncertainty (TPU) in the form of standard uncertainty, which takes all relevant uncertainty sources into account, can be obtained as,

$$u_y = \sigma_y = \sqrt{\left(\frac{\partial f}{\partial x_1}\right)^2 \sigma_1^2 + \left(\frac{\partial f}{\partial x_2}\right)^2 \sigma_2^2 + \dots \left(\frac{\partial f}{\partial x_n}\right)^2 \sigma_n^2 + \sum_{i=1}^n \sum_{j=1, i \neq j}^n \frac{\partial f}{\partial x_i} \frac{\partial f}{\partial x_j} \sigma_{i,j}} \quad (1.4)$$

where σ_i^2 is the variance of the i^{th} random variable, and $\sigma_{i,j}$ is the covariance of the i^{th} and j^{th} random variables.

Equation (1.4) can also be expressed in vector-matrix notation:

$$\sigma(y)^2 = AC_X A^T \quad (1.5)$$

$$A = \left[\frac{\partial f}{\partial x_1} \quad \frac{\partial f}{\partial x_2} \cdots \frac{\partial f}{\partial x_n} \right]$$

$$C_X = \begin{bmatrix} \sigma_1^2 & \sigma_{1,2} & \cdots & \sigma_{1,n} \\ \sigma_{2,1} & \sigma_2^2 & \cdots & \sigma_{2,n} \\ \vdots & \vdots & & \vdots \\ \sigma_{n,1} & \sigma_{n,2} & \cdots & \sigma_n^2 \end{bmatrix}$$

If the n input quantities are independent, then y 's uncertainty can be computed by

$$u_y = \sigma_y = \sqrt{\left(\frac{\partial f}{\partial x_1}\right)^2 \sigma_1^2 + \left(\frac{\partial f}{\partial x_2}\right)^2 \sigma_2^2 + \dots + \left(\frac{\partial f}{\partial x_n}\right)^2 \sigma_n^2} \quad (1.6)$$

since $\sigma_{i,j} = 0$ ($i \neq j$).

The partial derivatives show the effects of each input quantity on the final results, and are therefore often called sensitivity coefficients.

The expanded uncertainty, which defines a confidence interval (CI) about the measurement result within a percentage (%) possibility that the true value of the measurand lies, can be given by the product of the standard uncertainty and the coverage factor t which depends on the confidence level and the particular distribution:

$$U(y) = t \cdot u(y) \quad (1.7)$$

A 95% confidence level is commonly used in practice, with coverage factor 1.96 for normally distributed measurement,

$$U_{95}(y) = 1.96u(y) \quad (1.8)$$

1.3.2.2 Monte Carlo Method

It is often difficult to use analytical methods to estimate the uncertainty of complex measurement systems. The Monte Carlo method was devised to solve some difficult deterministic problems by running random simulations many times to obtain the distribution of the probabilistic outputs (Papadopoulos and Yeung, 2001). The concept behind the Monte Carlo method is to generate a large number of experimental trials from which the distribution function of the output quantity can be estimated. When applied to uncertainty analysis, one form of the Monte Carlo method is:

- (1) A sample of n input quantities $\{x_1, x_2, \dots, x_n\}$ is generated m times based on the probability density function of each input quantity (or the joint distribution of all the input quantities, if known).
- (2) The output for each set of input quantities can be obtained,

$$y_j = f(x_{1,j}, x_{2,j}, \dots, x_{n,j}) \quad (1.9)$$

for $j = 1, 2, \dots m$.

- (3) The probability density function of y can be estimated from $y_1, y_2 \dots y_m$. From this, the uncertainty of y can be also obtained.

Compared with the analytical method, the Monte Carlo method has some advantages. For example: (1) it is not necessary to compute complex partial derivatives; (2) it takes care of the dependencies of input quantities; and (3) it can deal with small and large uncertainties of input quantities (Papadopoulos and Yeung, 2001). Its biggest drawback is the computational cost. More realizations in the Monte Carlo simulations will provide a more accurate solution, but computation time will increase.

1.4 Previous Studies for Shoreline Uncertainty Analysis

To date, NGS does not have a statistical uncertainty model for photogrammetry-derived shorelines. Instead, field-survey-based methods have been used to evaluate the photogrammetry-derived shoreline uncertainty. In addition, empirical methods and stochastic methods are used for LiDAR-derived shoreline uncertainty (White *et al.*, 2011).

1.4.1 Field-Survey-Based Method for Photogrammetry-Derived Shoreline Uncertainty

The field-survey-based method has been used to estimate the uncertainty of photogrammetry-derived shoreline. Surveyors walk along the interface of land and water and use GPS to measure the three-dimensional coordinates of the interface points at the time when aerial images are taken (Figure 1.8). The shoreline generated by connecting these points is considered as the “true” shoreline and then compared with the

photogrammetry-derived shoreline to compute the uncertainty of the photogrammetry-derived shoreline (Hutchins, 1994).



Figure 1.8 Field-survey-based method for assessing the photogrammetry-derived shoreline uncertainty

This method has some drawbacks: (1) this field-survey-based method requires a large-scale deployment, which makes it impractical to conduct this method with each photogrammetric shoreline project; (2) it cannot provide sensitivity analysis (the influence of different factors on the final result), and it is not known how to control or decrease the uncertainty; and (3) the GPS-measured shoreline is not the actual true MHW or MLLW line. The instantaneous shoreline most likely will not be the same as the MHW or MLLW line due to some dynamic effects. In addition, GPS measurement still has uncertainty.

1.4.2 Empirical Method for LiDAR-Derived Shoreline Uncertainty

In 2008, NGS used a Topcon Laser-Zone integrated laser level and real-time GPS systems to assess the uncertainty of the LiDAR-derived shoreline along the North Carolina Outer Banks (White *et al.*, 2011). The coordinates of points near the shoreline were measured at a spacing of ~5m along each transect, which was oriented perpendicular to the shoreline. The spacing between transects was ~10m. The MHW zero-crossing points were

interpolated from the measured points. Finally, the spatial (Euclidean) distance from these MHW zero-crossing points to the points on the LiDAR-derived shoreline vector was computed to estimate the shoreline uncertainty.

The main benefit of this method is that it is independent of the data, whose uncertainty is assessed by it. However, this method has also the same drawbacks as the field-survey-based method for photogrammetry-derived shoreline. Therefore, as the IHO S-44 specifications mandates, a statistical method should be adopted to determine positioning uncertainty by combining all uncertainty sources (IHO, 2008).

1.4.3 Monte Carlo Simulation Method for LiDAR-Derived Shoreline Uncertainty

A Monte Carlo simulation method for topographic LiDAR-derived shoreline uncertainty was developed by White *et al.* (2011). The ranges and angles of the transmitted light pulses were acquired by back-projecting the laser geolocation equation (Lindenberger, 1989; Vaughn *et al.*, 1996; Filin, 2001) with the known coordinates of the ground points and the known positions and orientations of the LiDAR sensor. Based on the uncertainties of positions, attitudes, ranges and angles, a series of plausible estimates of these variables were formed. Through the process of normal geolocation, Digital Terrain Model (DTM) construction and shoreline extraction, a series of shorelines were then extracted to analyze the shoreline uncertainty.

This simulation method satisfies the IHO S-44 standards, and it is a statistical method, which does not require expensive field surveys. In addition, it can perform sensitivity analysis, through which users can know how each factor influences the final shoreline

uncertainty. However, this method has not been extended to the photogrammetry-derived shoreline uncertainty analysis.

1.5 Research Goals

Photogrammetric stereo compilation is the main shoreline mapping method used by NGS. Based on the review provided above, there is no adopted statistical method to estimate the photogrammetry-derived shoreline uncertainty. With this as an objective, this research provides a discussion of uncertainties involved in photogrammetric shoreline mapping and develops a TPU model in order to: (1) generate accuracy metadata for the national shoreline; (2) satisfy IHO S-44 Standards for Hydrographic Surveys; (3) help to make informed policy decisions; and (4) enable computation of uncertainty in shoreline change rate estimates and other derived data products.

1.6 Thesis Outline

The remainder of this thesis is organized as follows. Chapter 2 describes the study site and data. Chapter 3 presents the photogrammetry-derived shoreline uncertainty analysis for two cases: first, where the main uncertainty components for tide-coordinated imagery include exterior orientation element uncertainty, offset between MHW or MLLW datum and observed water level, uncertainty in water level data and human compilation uncertainty; and second, where the main uncertainty components for non-tide-coordinated imagery include exterior orientation element uncertainty, uncertainty in water level data and human compilation uncertainty. Chapter 4 discusses experimental results for the study

area. Chapter 5 contains an in-depth discussion of the results. Finally, chapter 6 contains conclusions and recommendations for future work.

CHAPTER 2 - STUDY SITE AND STUDY DATA

2.1 Study Site

On June 21st 2011, a NOAA NGS aerial survey (ME1001) was conducted to provide aerial images of the strait that links Dennys Bay, Whiting Bay and Cobscook Bay in the northeast coastal region of Maine, and this survey also covered other bays, entrances, and tributaries to the project area (Figure 2.1).

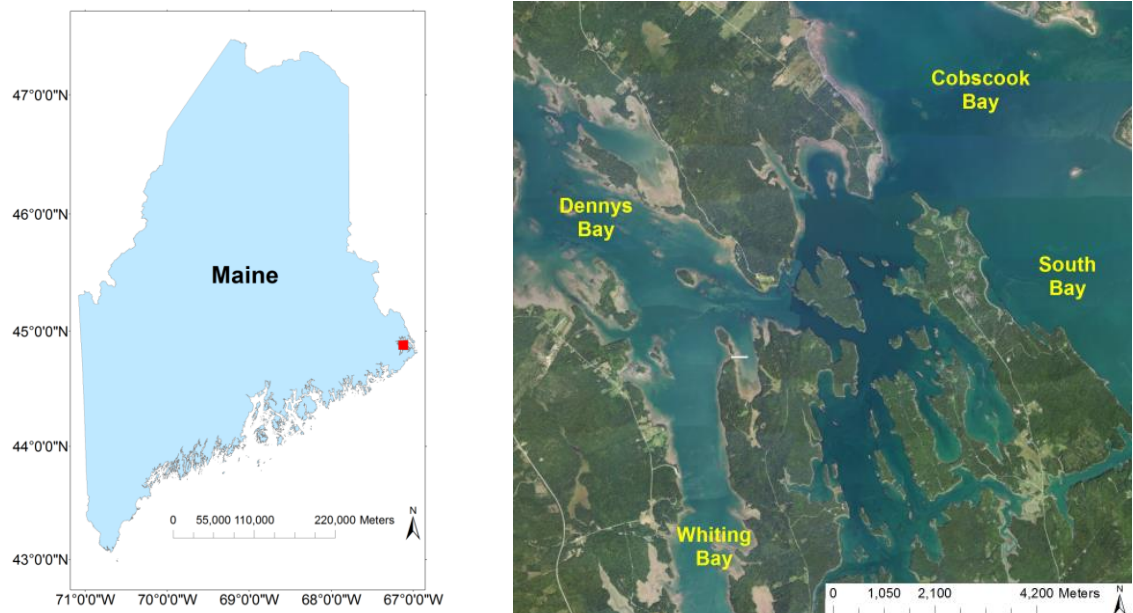


Figure 2.1 The survey area for ME1001. (Left) The blue area is the state of Maine, and the red box is the survey area; (right) The imagery of the survey area from ArcGIS imagery basemap

The region is characterized by a large tide range and strong tidal currents with an average tide range at Cobscook Bay of 7.3 m (which can exceed 8.5 m during spring tide).

Typically, a large volume of sea water flows in and out of it twice daily, which creates significant currents (NOAA Fisheries, 2014). The current can exceed 1.5 m/s (Xu *et al.*, 2006). Figure 2.2 shows the high tide and the low tide at Cobscook Bay. The study site contains numerous embayments (right image in Figure 2.1). The shoreline along the study site contains a wide range of beach slopes. Based on an analysis using ArcGIS and LiDAR data download from Digital Coast (Coastal Service Center, 2013), the slope range in the study site ranges from 1° to 46°, with the average slope being ~14°. The shoreline can be segmented into different types of convoluted shorelines, ranging from rock outcrops to gravel pocket beaches and tidal mudflats. The complexity of the site and the range of shoreline types covered were determined to be advantageous for developing the shoreline TPU model. In particular, it should be possible to extend the TPU model and procedures to other project sites that are less complex and exhibit greater homogeneity of shoreline type, whereas the reverse would not necessarily be true. It is also important to note that, due to the complexity of the shoreline in this region, the shoreline uncertainty is expected to generally be higher than that in other areas.



Figure 2.2 The tides at Cobscook Bay. (Left) High tide at 2:25 pm on September 19th, 2012; (right) low tide at 9:36 am on September 20th, 2012 (Courtesy of Kinexxions, 2014)

2.2 Study Data

2.2.1 Aerial Imagery

Seventy natural color and NIR images were taken using an Applanix Digital Sensor System (DSS) 439 DualCam at an altitude of 3048 m along two flight lines 50-001 and 50-002 (each flown twice). The mosaic natural color imagery, the flight lines and the tide gauges are depicted in Figure 2.3. Figure 2.4 is the mosaic NIR imagery. Table 2.1 provides the image acquisition parameters. In addition, a custom exterior orientation element report was output from POSPac (Applanix software for direct georeferencing of airborne imaging sensors (Applanix, 2013)) containing the exterior orientation elements of each image and also their standard uncertainties.

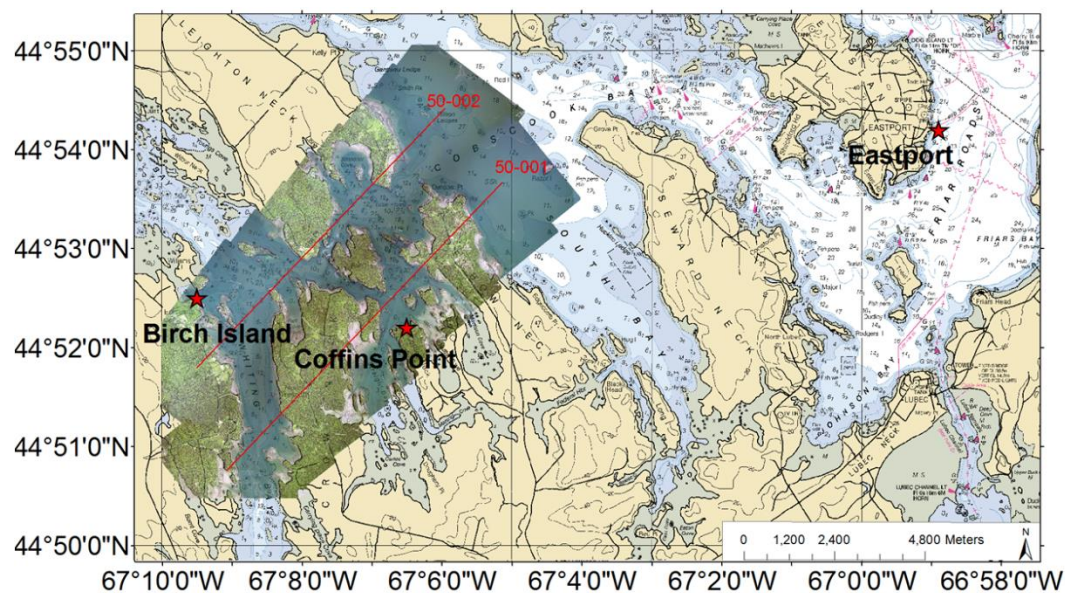


Figure 2.3 The mosaic natural color imagery overlaid on NOAA Chart (Office of Coast Survey, 2013b) (The red lines are the two flight lines. The red stars are the three tide gauges used in this survey)

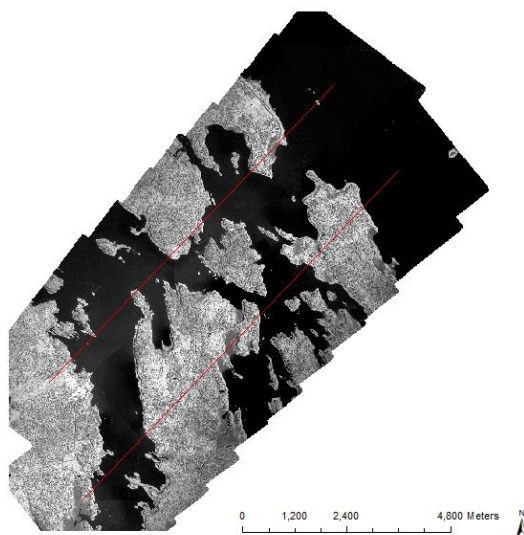


Figure 2.4 The mosaic near infrared imagery

Table 2.1 Image acquisition parameters

| | |
|--|---------------------|
| Flying height | 3048 m (10000 feet) |
| Camera focal length | 60.265 mm |
| Pixel size on CCD chip | 6.8 μ m |
| CCD length in the along-track direction | 5408 pixels |
| CCD length in the across-track direction | 7212 pixels |

2.2.2 Water Level Data

The tide gauges used for this survey were Coffins Point and Birch Island (both subordinate stations), and Eastport (19-year control station).

An NGS compiler performed tidal level calculations by applying the tidal correctors (time difference and range ratio) to Eastport's observations downloaded from the NOAA

Tides&Currents website (CO-OPS, 2014), and then produced the “Tide Analysis Report” (Table 2.2).

Table 2.2 Tide Analysis Report (provided by NGS)

| | | | | | | | | |
|--|----------------------|-----------------|-----------------|-----------------|---------------------|-----------------|-----------------|-----------------|
| The center time (GMT) of the flight line | 13:18 50- 002 | 13:24 50-001 | 14:06 50-001 | 14:18 50-002 | 13:18 50- 002 | 13:24 50-001 | 14:06 50-001 | 14:18 50-002 |
| | Relative to MLLW (m) | | | | Relative to MHW (m) | | | |
| Eastport | 0.39 | 0.35 | 0.33 | 0.40 | -5.34 | -5.38 | -5.40 | -5.33 |
| Coffins Point | 0.59 | 0.58 | 0.27 | 0.27 | -4.84 | -4.84 | -5.16 | -5.16 |
| Birch Islands | 1.10 | 0.88 | 0.36 | 0.30 | -4.33 | -4.54 | -5.07 | -5.13 |

Given that the tide tolerance for the two subordinate stations is 0.53 m (the mean tide ranges for Coffins Point and Birch Islands are 5.3m), two of the four flight lines were out of the MLLW tide tolerance, and all the flight lines were out of the MHW tide tolerance. Thus, the MLLW shorelines were mainly compiled from tide-coordinated imagery, and all the MHW shorelines were from non-tide-coordinated imagery. This situation provided a good test case for the study, since uncertainties in both methods of shoreline compilation (tide-coordinated and non-tide-coordinated) could be assessed.

In addition, the NOAA Tides&Currents web service provided predicted data for Coffins Point based on harmonic constituents and predicted data for Birch Islands based on four time and range correction parameters.

2.2.3 Compiled Shorelines

MHW and MLLW lines in ArcGIS shapefile format over the study site were downloaded from NOAA Shoreline Data Explorer (NGS, 2014d). The shoreline compilation was conducted from interpreted imagery according to standard digital photogrammetric procedures in 2012. As “Scope of Work for Shoreline Mapping under the NOAA Coastal Mapping Program” specifies (Leigh *et al.*, 2012), MLLW lines should be only delineated over soft bottom areas or around man-made features with gentle slope into the water. In addition, the furthest extent of exposed bare ground at low tide is required to be greater than 1 mm from the shoreline at the compilation scale. According to these MLLW line compilation requirements, the MLLW lines in some areas may be interpreted as other NGS shoreline attributes, such as Ledge.Submerged or Ledge.Covers/Uncovers. This also explains why the MLLW lines in Figure 2.5 are not continuous.

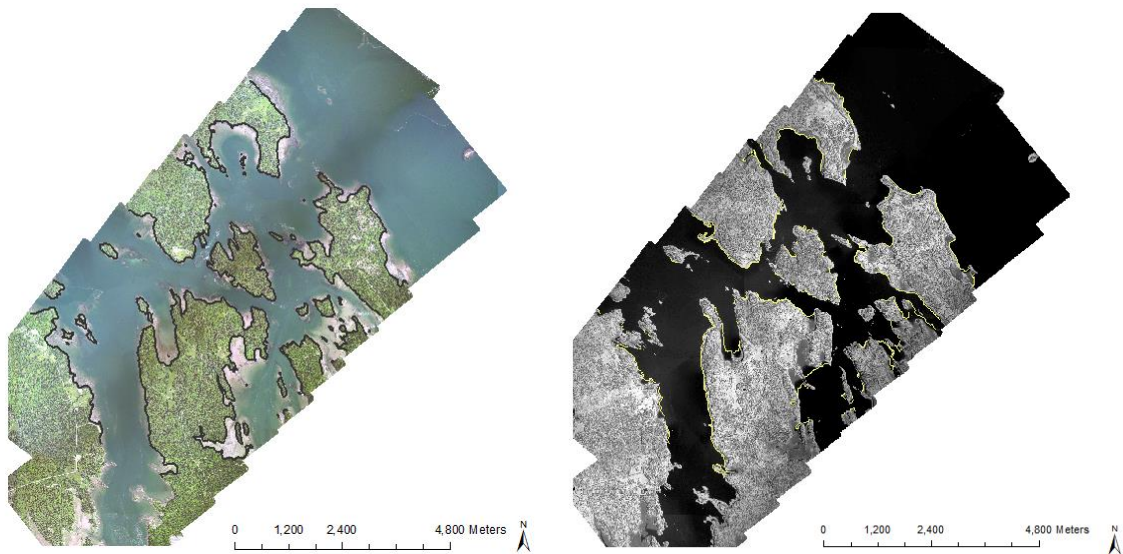


Figure 2.5 MHW and MLLW lines for the survey area. (Left) The black lines are MHW lines; (Right) the yellow lines are MLLW lines

In order to analyze the human compilation uncertainty, shorelines from different compilers should be obtained. Due to lack of the MLLW compilation results (from different compilers) based on tide-coordinate imagery in the study area, an alternative data set was used. The alternative dataset included compiled land/water interface vectors from four compilers in the Fort Desoto, Florida project from 2003 (Parrish *et al.*, 2005) and was applied in this study in order to estimate the human compilation uncertainty for the tide-coordinated case. Table 2.3 represents the compilation result analysis from the four compilers based on the comparison between the compiled shorelines and the GPS ground truth. Given that the coastal region of Fort Desoto is less complex than the study site of Maine, the human compilation uncertainty for Fort Desoto may underestimate that for Maine. In addition, the sample size (only four compilers) is small. These are limitations of using the Fort Desoto to analyze human compilation uncertainty for the Maine study site. However, this was the best available data set for this portion of the analysis.

Table 2.3 Compilation result analysis for 2003 Fort Desoto, Florida project

| Shoreline | Mean (m) | RMSE (m) |
|------------|----------|----------|
| Compiler 1 | -0.59 | 0.94 |
| Compiler 2 | -1.56 | 1.94 |
| Compiler 3 | -0.39 | 0.92 |
| Compiler 4 | -0.98 | 1.45 |

For the analysis of the non-tide-coordinated human compilation uncertainty, nine NGS compilers with different experience levels compiled the MHW lines from non-tide-coordinated imagery in two selected areas (Figure 2.6 and Figure 2.7).



Figure 2.6 Two selected areas for non-tide-coordinated human compilation uncertainty analysis (red boxes)

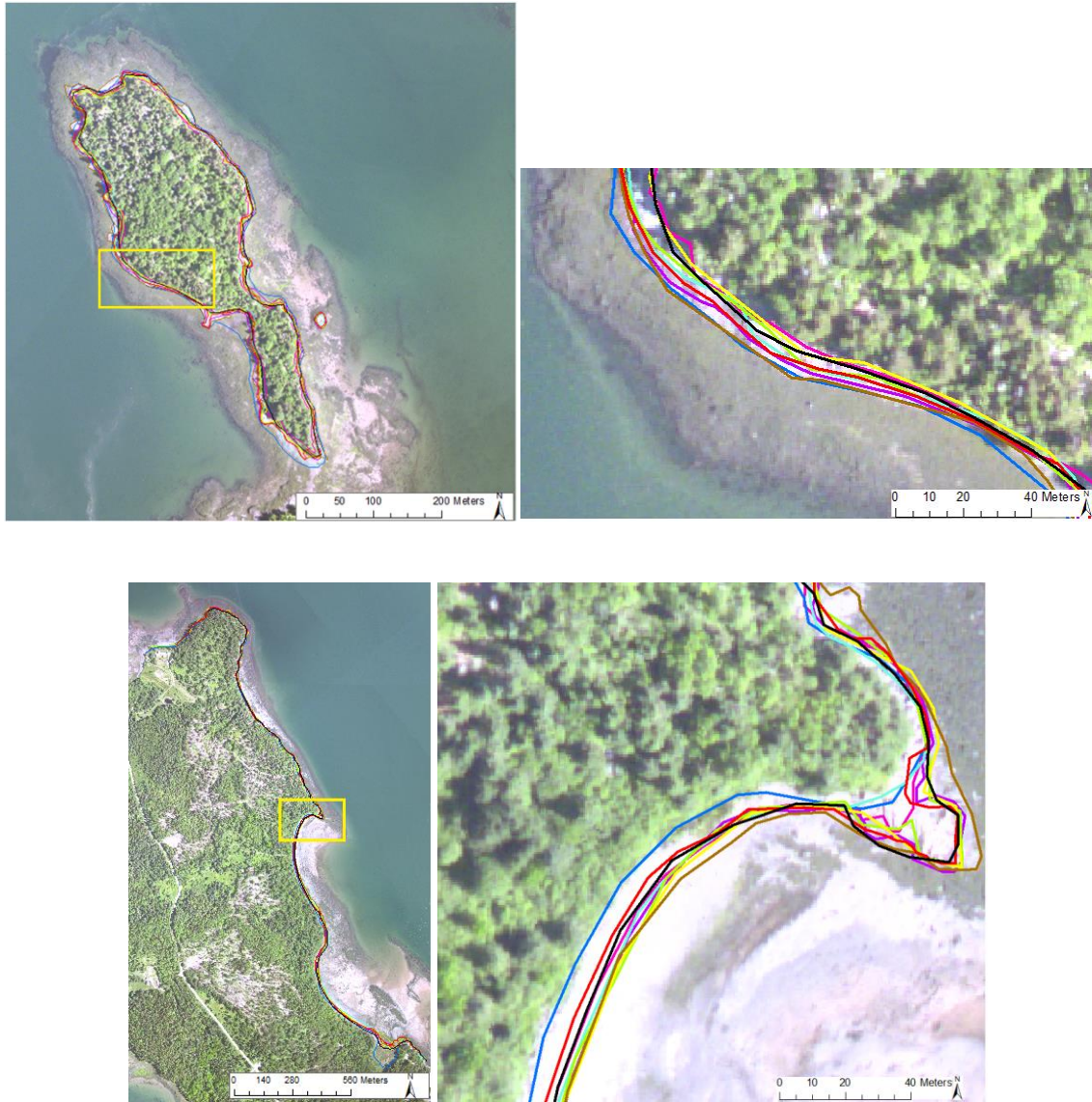


Figure 2.7 Compiled MHW lines from 9 compilers

2.2.4 LiDAR Data

LiDAR topographic data were collected at a 2 m nominal point spacing for coastal Maine as part of 2010 U.S. Geological Survey (USGS) American Recovery and Reinvestment Act (ARRA) LiDAR project, while there was no snow on the ground and water was at or below normal levels. The vertical accuracy of the data is 0.15 m.

The LiDAR data over the study site were downloaded from the Digital Coast web service (Coastal Services Center, 2013) and were applied to extract the beach slope. This data set is a raster image file of Z values (GeoTiff format) with a grid cell size of 3 m by 3 m.

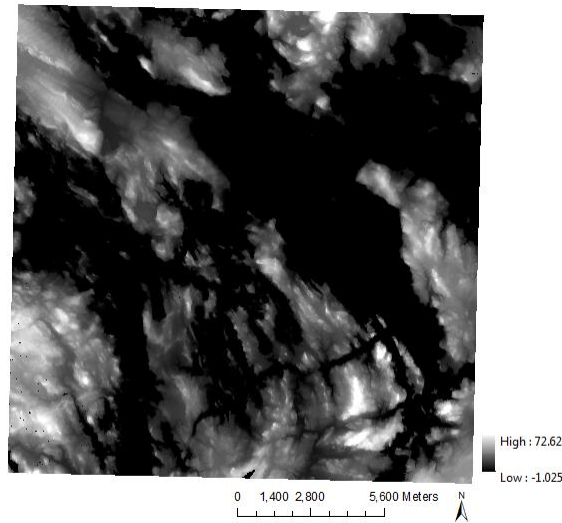


Figure 2.8 LiDAR data for the ME1001 survey area

CHAPTER 3 - PHOTOGRAMMETRY-DERIVED SHORELINE UNCERTAINTY ANALYSIS

Although the photogrammetric stereo compilation technology is well understood for terrain analysis over dry areas away from the coast (McGlone *et al.* 2004), measurement and compilation uncertainties are still not adequately modeled in shoreline mapping. This chapter will discuss the uncertainty components and the total propagated uncertainty model for tide-coordinated and non-tide-coordinated shoreline mapping. As described in section 3.1, the main uncertainty components for tide-coordinated shoreline mapping include exterior orientation element uncertainty, offset between MHW or MLLW datum and observed water level, uncertainty in water level data, and human compilation uncertainty. As described in section 3.2, the main uncertainty components for non-tide-coordinated shoreline mapping include exterior orientation element uncertainty, uncertainty in water level data, and human compilation uncertainty.

3.1 Shoreline Uncertainty based on Tide-Coordinated Imagery

3.1.1 Exterior Orientation Element Uncertainty

In order to derive three-dimensional ground coordinates from two-dimensional image space, the photogrammetric mapping workflow includes: interior orientation, relative orientation, absolute orientation, and feature extraction (McGlone *et al.*, 2004). Interior

orientation establishes the relationship between the pixel and the image coordinate system. Relative orientation determines the relative position and orientation of two overlapping images with respect to one another by measuring some corresponding image points in the overlapping area of the images. Absolute orientation establishes the relationship between the image coordinate system and the object space coordinate system by acquiring the position and attitude of each exposure station which are represented by six exterior orientation elements: X_L , Y_L , Z_L , ω , φ , κ . In absolute orientation, ground control points are generally required. After exterior orientation elements are obtained, ground point coordinates are acquired by intersecting two corresponding rays from two exposure stations, and then feature extraction can be implemented. The following collinearity equations present the relationship among exposure stations, image points and ground points.

$$X - X_{L1} = (Z - Z_{L1}) \frac{m_{11,1}(x_1 - x_0) + m_{21,1}(y_1 - y_0) + m_{31,1}(-f)}{m_{13,1}(x_1 - x_0) + m_{23,1}(y_1 - y_0) + m_{33,1}(-f)} \quad (3.1)$$

$$Y - Y_{L1} = (Z - Z_{L1}) \frac{m_{12,1}(x_1 - x_0) + m_{22,1}(y_1 - y_0) + m_{32,1}(-f)}{m_{13,1}(x_1 - x_0) + m_{23,1}(y_1 - y_0) + m_{33,1}(-f)} \quad (3.2)$$

$$X - X_{L2} = (Z - Z_{L2}) \frac{m_{11,2}(x_2 - x_0) + m_{21,2}(y_2 - y_0) + m_{31,2}(-f)}{m_{13,2}(x_2 - x_0) + m_{23,2}(y_2 - y_0) + m_{33,2}(-f)} \quad (3.3)$$

$$Y - Y_{L2} = (Z - Z_{L2}) \frac{m_{12,2}(x_2 - x_0) + m_{22,2}(y_2 - y_0) + m_{32,2}(-f)}{m_{13,2}(x_2 - x_0) + m_{23,2}(y_2 - y_0) + m_{33,2}(-f)} \quad (3.4)$$

$$M = \begin{bmatrix} m_{11} & m_{12} & m_{13} \\ m_{21} & m_{22} & m_{23} \\ m_{31} & m_{32} & m_{33} \end{bmatrix}$$

$$m_{11} = \cos \varphi \cos \kappa$$

$$m_{12} = \cos \omega \sin \kappa + \sin \omega \sin \varphi \cos \kappa$$

$$m_{13} = \sin \omega \sin \kappa - \cos \omega \sin \varphi \cos \kappa$$

$$m_{21} = -\cos \varphi \sin \kappa$$

$$m_{22} = \cos \omega \cos \kappa - \sin \omega \sin \varphi \sin \kappa$$

$$m_{23} = \sin \omega \cos \kappa + \cos \omega \sin \varphi \sin \kappa$$

$$m_{31} = \sin \varphi$$

$$m_{32} = -\sin \omega \cos \varphi$$

$$m_{33} = \cos \omega \cos \varphi$$

where (X, Y, Z) are the ground point coordinates, (x_1, y_1) and (x_2, y_2) are the image space coordinates of the corresponding image points on image 1 and image 2, f is the focal length, (X_{L1}, Y_{L1}, Z_{L1}) and (X_{L2}, Y_{L2}, Z_{L2}) are the coordinates of exposure station 1 and exposure station 2, the rotation matrix M is given by Eq. 4-18b of Mikhail *et al.* (2001), the elements of M are the functions of three exterior orientation angle elements $(\omega, \varphi, \kappa)$. (x_0, y_0) are the principal point offsets, and in this thesis we ignore their effect on the positioning accuracy and set $(x_0, y_0) = (0, 0)$. With known exterior orientation elements and measured corresponding image point coordinates, ground point coordinates can be estimated with the least square method based on the above four equations (Figure 3.1).

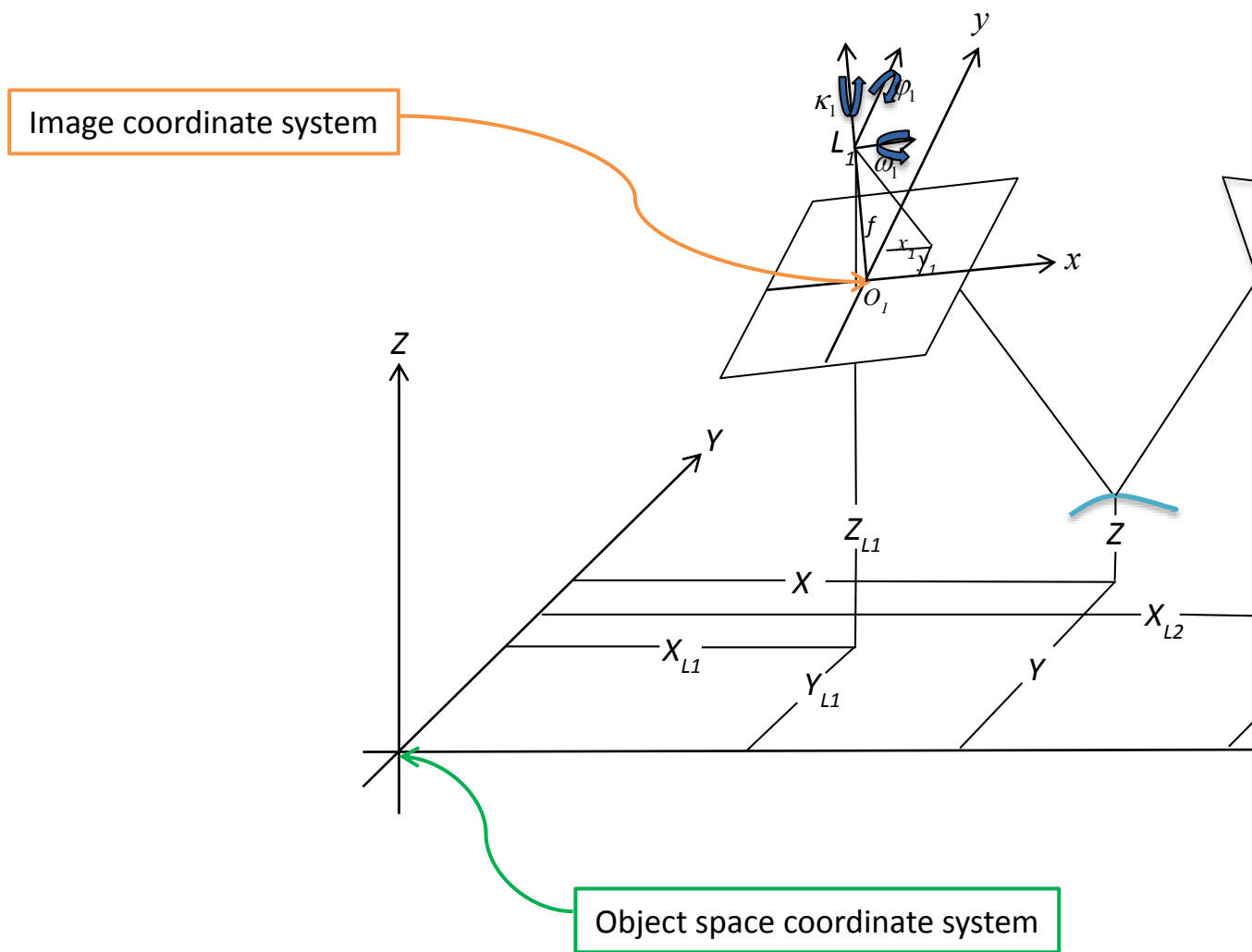


Figure 3.1 Space intersection

The use of an integrated GPS/IMU system makes direct georeferencing without ground control points possible in aerial photogrammetry (Schwarz *et al.*, 1993; Grejner-Brzezinska, 1999), as the system can provide accurate exterior orientation elements of exposure stations. Direct georeferencing overcomes some disadvantages of traditional aerial photogrammetry: complex workflow, inefficiency, and dependence on ground control points (Maune, 2007; Yuan and Zhang, 2008). With the wide application of direct georeferencing technology, estimates of the accuracy must be developed in order to (1)

determine if a given integrated GPS/IMU system can meet the need of the actual application prior to a survey; (2) provide accuracy metadata for a direct georeferencing result (White *et al.*, 2011); and (3) enable uncertainty analysis in downstream products (Parrish, 2011).

The uncertainty components in direct georeferencing mainly include: interior orientation element (x_0, y_0, f) uncertainty, exterior orientation element $(X_{L1}, Y_{L1}, Z_{L1}, \omega, \varphi, \kappa)$ uncertainty and uncertainty of corresponding image point coordinate measurement. The influence of interior orientation element uncertainty on direct georeferencing accuracy is much smaller than that of exterior orientation element uncertainty, particularly with a well-calibrated camera (Zhang and Yuan, 2008). This thesis focuses on measurement and processing uncertainty, which is treated as first-order uncertainty. Calibration uncertainty is treated as second-order uncertainty and ignored in this thesis. The uncertainty of image point coordinate measurement can be treated as part of the human compilation uncertainty, which will be discussed later. Therefore, this section only focuses on exterior orientation element uncertainty.

Some researchers have analyzed the effect of exterior orientation element uncertainties on ground point positioning (Zhang and Yuan, 2008; Yuan and Zhang, 2008; Mostafa *et al.*, 2001). The uncertainty of direct georeferencing based on collinearity equations computed by error equations (Zhang and Yuan, 2008; Yuan and Zhang, 2008) is actually the least square estimation uncertainty rather than the positioning uncertainty caused by exterior orientation element uncertainties. Mostafa *et al.* (2001) analyzed the positioning accuracy of some POS/AVTM systems in different photographic scales based on standard error propagation theory. However, because ground point coordinates are estimated by the least

square method, the derivation of error propagation formula is quite complex and is easy to get wrong. Furthermore, during linearization the nonlinear model errors are introduced due to not taking some high order terms into account (Papadopoulos and Yeung, 2001). Therefore, the conventional uncertainty analysis method is not optimal for this problem. Currently, most relevant research estimates the final ground point positioning accuracy depending on some measured corresponding image point coordinates. The positioning accuracy cannot be obtained without corresponding image point coordinate measurements using these methods. In this thesis, a Monte Carlo simulation method is developed to estimate the propagated uncertainty in ground point coordinates caused by exterior orientation element uncertainties, and no measured corresponding image point coordinates are needed in this method.

For a specific direct georeferencing survey, with the exterior orientation elements and their uncertainties of each image known, the ground point positioning uncertainty for the whole survey area can be obtained by computing the root mean square (RMS) of the uncertainties of all the stereo image pairs. The steps of the uncertainty computation method for each stereo image pair are as follows:

- (1) One hundred equally spaced image points are selected from image 1. For each image point, the uncertainty computation steps are from (2) to (7).
- (2) With the known exterior orientation elements of image 1 (Y_{L1} , Z_{L1} , ω_1 , φ_1 , κ_1), the image point coordinates (x_1, y_1) and the average elevation of the survey area, estimate the corresponding ground point coordinates (X, Y, Z) by the collinearity equations.

- (3) Obtain a series of the possible exterior orientation elements of image 1 and image 2 ($X_{L1}', Y_{L1}', Z_{L1}', \omega_1', \varphi_1', \kappa_1'$ and $X_{L2}', Y_{L2}', Z_{L2}', \omega_2', \varphi_2', \kappa_2'$, respectively) using a Gaussian probability distribution centered on the reported values ($X_{L1}, Y_{L1}, Z_{L1}, \omega_1, \varphi_1, \kappa_1$) and ($X_{L2}, Y_{L2}, Z_{L2}, \omega_2, \varphi_2, \kappa_2$) with the uncertainties ($\sigma_{X_{L1}}, \sigma_{Y_{L1}}, \sigma_{Z_{L1}}, \sigma_{\omega_1}, \sigma_{\varphi_1}, \sigma_{\kappa_1}$) and ($\sigma_{X_{L2}}, \sigma_{Y_{L2}}, \sigma_{Z_{L2}}, \sigma_{\omega_2}, \sigma_{\varphi_2}, \sigma_{\kappa_2}$) as the standard deviations (Liu *et al.*, 2007).
- (4) With the true exterior orientation element values ($X_{L1}', Y_{L1}', Z_{L1}', \omega_1', \varphi_1', \kappa_1'$) and ($X_{L2}', Y_{L2}', Z_{L2}', \omega_2', \varphi_2', \kappa_2'$), compute the corresponding image point coordinates (x_1', y_1') and (x_2', y_2') of the ground point (X, Y, Z).
- (5) Compute the ground point coordinates (X', Y', Z') using (x_1', y_1'), (x_2', y_2') and the reported exterior orientation elements.
- (6) Repeat steps (4) and (5) N times to get a series of possible ground point coordinates.
- (7) Calculate the uncertainty of the ground point coordinates according to the distribution of all the possible positions.
- (8) Obtain the point positioning uncertainty of each image pair by calculating summary uncertainty statistics of all image points.

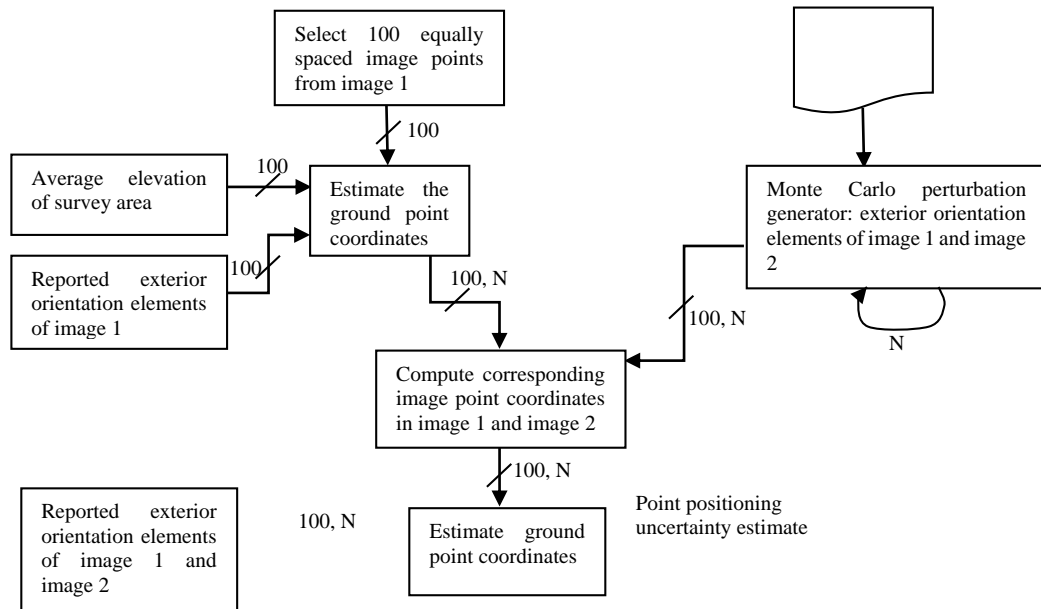




Figure 3.2 Configuration of the Monte Carlo analysis method for determining positioning uncertainty caused by exterior orientation element uncertainty for each image pair

Compared with the conventional uncertainty analysis method, the Monte Carlo simulation method is simple theoretically, and it does not require the complex partial derivatives of the ground point coordinates with respect to each exterior orientation element. However, this method is more costly computationally. Although a larger number of realizations will provide a more accurate final result, the processing time will also increase.

To summarize the uncertainty, the distance root mean square (DRMS) is computed as the position uncertainty caused by exterior orientation element uncertainty according to:

$$DRMS = \sqrt{\sigma_x^2 + \sigma_y^2} \quad (3.5)$$

where σ_x and σ_y are the standard uncertainty of X and Y coordinates respectively.

3.1.2 Offset between MHW or MLLW Datum and Observed Water Level

Compilers interpret the land-water interface as MHW or MLLW shoreline on tide-coordinated imagery, under the assumption that the water level at the time of image acquisition is at the MHW or MLLW datum, or the offset between them is within the desired tolerance. Actually, imagery can rarely be taken at the time when the observed water level is exactly coincident with the MHW or MLLW datum. When considering shoreline uncertainty, the offset between them cannot be ignored.

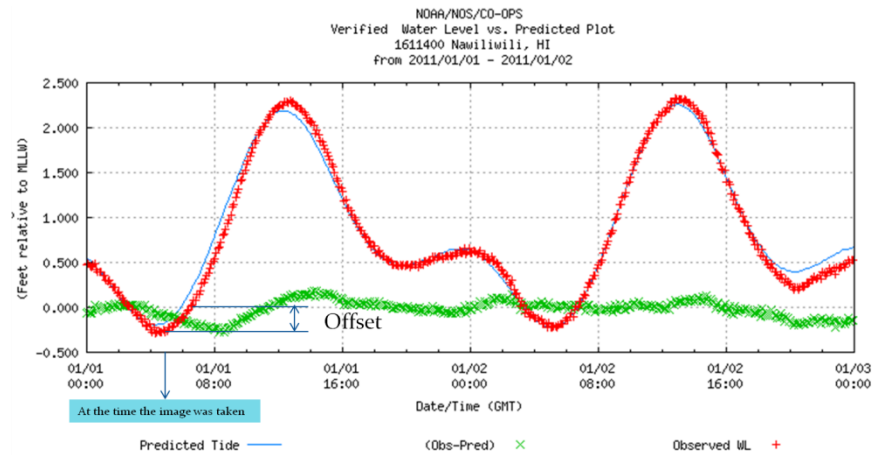


Figure 3.3 Offset between the observed water level and MLLW datum at the time the image was taken

In order to estimate water level data for the interested area, the two primary methodologies of tidal zoning are applied by NOAA: discrete tidal zoning and Tidal Constituent and Residual Interpolation (TCARI). Discrete tidal zoning uses polygons to define geographic areas of similar tidal characteristics. In each polygon, the same tidal correctors (time difference and range ratio) from tide stations are applied to obtain the water level data for the area. TCARI creates a triangulated mesh for the coastal area of interest, and then interpolates the water level by a set of weighting functions applied to the astronomic tide (each tidal constituent's amplitude and phase value), residual (the observed water level value minus the predicted water level value), and datum offset (Mean Sea Level (MSL) minus MLLW) based on data at the tide stations (Office of Coast Survey, 2013c).

If TCARI grids are available, NGS will use the Pydro software package (Office of Coast Survey, 2013d) to find the instantaneous water level relative to MHW and MLLW at the time of acquisition of each image (Figure 3.4). Otherwise, CO-OPS develops discrete tidal zoning schemes to estimate the water level data.

| Image ID | Water Level relative to MHW | Water Level relative to MLLW | Date | Image ID |
|-------------|-----------------------------|------------------------------|--------|----------|
| 330021_0384 | -2.25 | -0.02 | 06AR03 | 30-021 |
| 330021_0385 | -2.33 | -0.06 | 06AR03 | 30-021 |
| 330021_0386 | -2.41 | -0.10 | 06AR03 | 30-021 |
| 330021_0387 | -2.47 | -0.12 | 06AR03 | 30-021 |
| 330021_0388 | -2.44 | -0.11 | 06AR03 | 30-021 |
| 330021_0389 | -2.44 | -0.11 | 06AR03 | 30-021 |
| 330021_0390 | -2.43 | -0.10 | 06AR03 | 30-021 |
| 330021_0391 | -2.43 | -0.10 | 06AR03 | 30-021 |
| 330021_0392 | -2.43 | -0.09 | 06AR03 | 30-021 |
| 330021_0393 | -2.42 | -0.09 | 06AR03 | 30-021 |
| 330018_0394 | -2.63 | -0.44 | 06AR03 | 30-018 |
| 330018_0395 | -2.60 | -0.39 | 06AR03 | 30-018 |
| 330018_0396 | -2.60 | -0.39 | 06AR03 | 30-018 |
| 330018_0397 | -2.35 | -0.03 | 06AR03 | 30-018 |
| 330018_0398 | -2.34 | -0.03 | 06AR03 | 30-018 |
| 330018_0399 | -2.32 | -0.02 | 06AR03 | 30-018 |
| 330018_0400 | -2.31 | -0.01 | 06AR03 | 30-018 |
| 330018_0401 | -2.30 | -0.01 | 06AR03 | 30-018 |
| 330018_0402 | -2.25 | 0.02 | 06AR03 | 30-018 |
| 330018_0403 | -2.16 | -0.02 | 06AR03 | 30-018 |
| 330018_0404 | -2.14 | 0.00 | 06AR03 | 30-018 |
| 330018_0405 | -2.10 | 0.03 | 06AR03 | 30-018 |
| 330018_0406 | -2.06 | 0.04 | 06AR03 | 30-018 |
| 330018_0407 | -2.04 | 0.04 | 06AR03 | 30-018 |
| 330018_0408 | -2.04 | 0.00 | 06AR03 | 30-018 |
| 330018_0409 | -1.84 | 0.14 | 06AR03 | 30-018 |
| 330018_0410 | -1.84 | 0.14 | 06AR03 | 30-018 |
| 330017_0411 | -2.09 | -0.01 | 06AR03 | 30-017 |
| 330017_0412 | -2.18 | -0.07 | 06AR03 | 30-017 |
| 330017_0413 | -2.34 | -0.19 | 06AR03 | 30-017 |
| 330017_0414 | -2.45 | -0.29 | 06AR03 | 30-017 |
| 330017_0415 | -2.51 | -0.33 | 06AR03 | 30-017 |

Figure 3.4 An example of Pydro-generated water level relative to MHW and MLLW at the time of acquisition of each image (second column: water level relative to MHW; third column: water level relative to MLLW; last column: image ID)

3.1.3 Uncertainty in Water Level Data

Even if the observed water level equals MHW or MLLW datum zero at the time of imagery acquisition, the actual water level may be different from the MHW or MLLW datum due to uncertainty in water level data. The water level uncertainty sources for the two tidal zoning methodologies mentioned in the section 3.1.2 are different.

TCARI: In the case of a survey area covered by TCARI grids, the water level uncertainty sources include: water level observation uncertainty, harmonic constant uncertainty, uncertainty in computation of tidal datum for the adjustment to a 19-year NTDE from short-term stations, and Laplace Equation interpolation uncertainty. Figure 3.5 shows all the contributing elements for TCARI water level uncertainty.

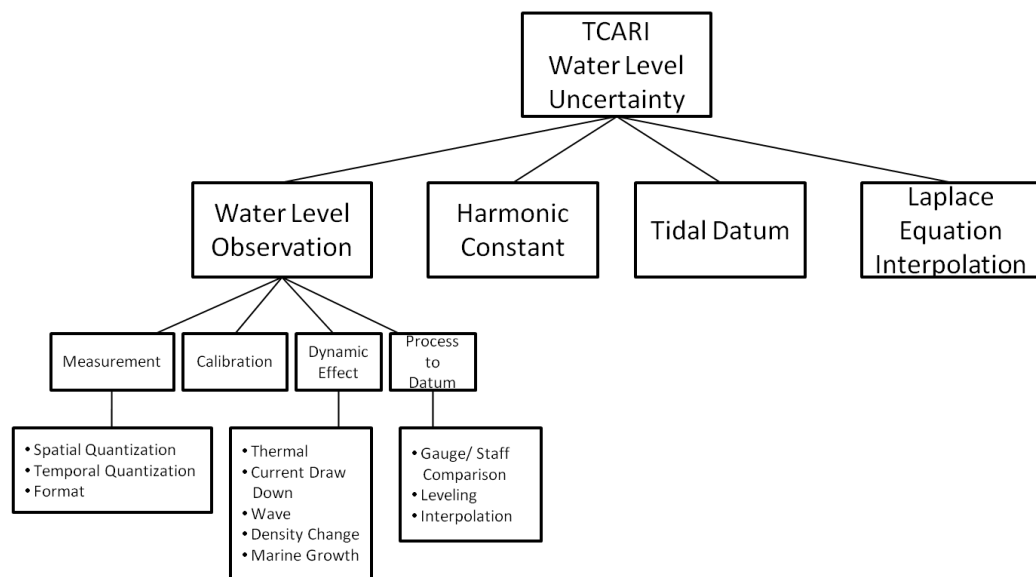


Figure 3.5 TCARI water level uncertainty (adapted from Brennan, 2005)

(1) Water level observation uncertainty

Gauges and sensors need to be calibrated, and the uncertainties due to dynamic effects should be reduced by sensor design and data sampling. In addition, the measurements need to be referenced to bench marks and tide staffs (Gibson and Gill, 1999). Therefore, water level observation uncertainty can be caused by measurement, calibration, dynamic effects, and processing to datum.

Measurement: any gauge/sensor can only collect water level data with finite resolution. The higher the resolution is, the smaller the vertical quantization uncertainty will be. Water

level is measured at an interval of 181 seconds (the average of 181 one-second interval water level samples) and reported every 6 minutes. This temporal quantization uncertainty is one source of measurement uncertainty, but it is very small (on the order of 10^{-5} m) and can be ignored (Brennan, 2005). In addition, the average of the 181 one-second interval measurements is rounded or truncated when it is recorded in the CO-OPS data collection platform. This format uncertainty is assumed to be the same as the reported highest resolution of the sensor.

Calibration: the water level sensor can be a self-calibrating acoustic, pressure, or other approved type. For different types of sensors, the calibration uncertainties are different. It was reported in Brennan (2005) that the agreement between a sensor and a reference must be less than 6×10^{-6} m.

Dynamic effects: dynamic effects on water level measurement include thermal, current draw down, wave, density change, and marine growth (Brennan, 2005).

Solar insolation variation may change the measurement accuracy from an acoustic sensor: 1) different temperatures results in different sound speeds along the sounding tube (Porter and Shih, 1996); 2) thermal expansion caused by solar insolation may change the length of sounding tube; and 3) the transducer gain may change due to different solar insolation. Some measures can be taken to reduce the uncertainty from thermal effect, such as keeping the acoustic transducer and stilling well in the same thermal condition, promoting air flow in the stilling well, and not making the sounding tube too long.

According to the Bernoulli principle, the presence of a stilling well changes the original water flow, which makes the water level inside the stilling well lower than the mean water

level around the stilling well (Shih and Baer, 1991). The current-induced uncertainty increases with the current speed. An engineering design (Figure 3.6) developed by NOAA can effectively reduce this uncertainty. When the current speed is less than 1.5 m/second, this design can reduce the current-induced uncertainty to a negligibly small value (Brennan, 2005).

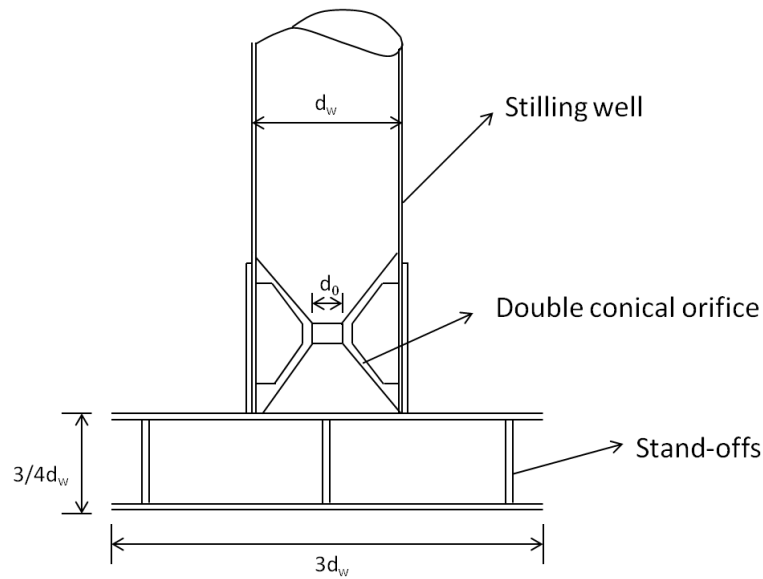


Figure 3.6 The tide gauge design used to reduce the current-induced uncertainty (adapted Shih *et al.*, 1984)

Waves may make orifice pressure fluctuate, which results in the change of gauge reference datum. When the significant wave height is greater than 2m, the typical value of the wave-induced uncertainty is 0.05m (personal communication, Stephen Gill, NOAA/NOS/CO-OPS, 2012). However, an orifice chamber with larger diameter can effectively control this uncertainty (Shih, 1986).

Tides can cause a change of water density. The water around the gauge during periods of high tide may be significantly denser than that during periods of low tide. The water inside the stilling well may be less dense than that outside, because the less dense water floods

into the stilling well at low tide and stays in the well until the water rises. The difference of density between inside and outside makes the pressure different, which will result in higher water inside the stilling well. The uncertainty due to density change is less than 0.03m, and its typical value is 0.01m (personal communication, Stephen Gill, NOAA/NOS/CO-OPS, 2012).

Furthermore, marine growth can affect water level measurement. If the orifice of the stilling well is blocked by marine growth, the amplitude and phase of water level measurement will be affected (Noye, 1974). This effect can be reduced or removed by maintenance of the tide gauge.

Processing to datum: the tide gauge should be referenced to the station datum through tide staffs, levels and bench marks. The maximum allowable closure error for the leveling loop is 0.01m (Brennan, 2005). For a pressure sensor gauge, a gauge-to-staff reading comparison may cause uncertainty. This uncertainty for an acoustic sensor gauge can be ignored because there is no gauge-to-staff reading comparison. Furthermore, in order to determine the water level data for an arbitrary time, the discontinuous water level samples need to be interpolated. The interpolation uncertainty is usually less than 0.03m, and its typical value is 0.01m (personal communication, Stephen Gill, NOAA\NOS\CO-OPS, 2012).

(2) Harmonic constant uncertainty

Astronomic tides can be decomposed into a series of harmonic constituents, which mainly account for the orbital motion of the Moon, the Earth, and the Sun. CO-OPS uses 37 constituents to predict astronomic tides. Each tidal constituent has two harmonic constants:

amplitude (cm) and phase (degrees). A least square analysis on water level observations can be performed to derive the harmonic constants, and each harmonic constant has an associated uncertainty.

Brennan (2005) applied a Monte Carlo simulation to calculate the uncertainties associated with the harmonic constants for nine stations which vary in latitude and longitude, and tide types. The range of the uncertainties associated with the harmonic constants for the nine stations are approximately from 0.02m to 0.25m. The investigation result showed if the record length used to compute harmonic constants was longer, the associated uncertainty would be smaller. Therefore, harmonic constant uncertainties for different stations are different, mainly depending on observation length.

(3) Tidal datum uncertainty

In the U.S. the National Water Level Observation Network (NWLON) is used to acquire and maintain the tidal datum reference framework. Tidal datums for many NWLON stations are computed by averaging the water level data over the 19-year NTDE from 1983 to 2001. For a short-term tide station, tidal datum is computed by comparing simultaneous water level data between the short-term tide station and the appropriate NWLON control station which is close to the short-term station and has similar tidal characteristics as the short-term station.

As the tidal datum computation for short-term stations is not based on the full 19-year NTDE observation, the tidal datum determination will bring in an uncertainty. Bodnar's equations (Bodnar, 1981) provide uncertainty estimations of MLW datum determination from short-term stations:

$$S_1 = 0.0021\Delta t + 0.0016\sqrt{\frac{d}{1852}} + 0.0092\left|\frac{r_c-r_s}{r_c}\right| + 0.0088 \quad (3.6)$$

$$S_3 = 0.0013\Delta t + 0.0011\sqrt{\frac{d}{1852}} + 0.0078\left|\frac{r_c-r_s}{r_c}\right| + 0.0088 \quad (3.7)$$

$$S_6 = 0.0006\Delta t + 0.0007\sqrt{\frac{d}{1852}} + 0.0063\left|\frac{r_c-r_s}{r_c}\right| + 0.0091 \quad (3.8)$$

$$S_{12} = 0.0025\sqrt{r_c + r_s} + 0.0390\left|\frac{r_c-r_s}{r_c}\right| + 0.0076 \quad (3.9)$$

where S_1 , S_3 , S_6 , and S_{12} are the standard uncertainty (in meters) for the short-term stations with one-month, three-month, six-month and 12-month observations respectively, Δt is the time difference of the low water intervals between control and short-term stations (in hours), d is the geographic distance between control and short-term stations (in meters), r_c and r_s are the mean range of tide at the control station and short-term station respectively (in meters) (Note that the constants and notations in these equations differ from those in Bodnar (1981), as metric units are used in this thesis).

The equations for MLLW datum are the same as those for MLW datum. Given that uncertainties for low water datums are higher than those for high water datums (NOAA, 2010), Bodnar's equations can be used to estimate the uncertainties for all tidal datums, and the actual uncertainty values should be less than the Bodnar-equation computed values.

According to Bodnar's equations, tidal datum uncertainty is a function of the time difference of low water intervals between control and short-term stations, the distance between control and short-term stations, and the mean tide ranges at control and short-term stations. In addition, it also depends on the time length of short-term station observation.

The longer the short-term station observation is, the smaller the tidal datum uncertainty will be. For stations with observation longer than one year, the tidal datum uncertainty can be time-interpolated between the uncertainty estimation for one-year observation and the zero value for 19-year NTDE observation (NOAA, 2010).

(4) Laplace Equation interpolation uncertainty

TCARI uses the Laplace Equation interpolation method to generate spatial weighting functions to interpolate: 1) tidal constants for reconstructing astronomic tide; 2) the residual caused by non-tidal effects; and 3) the datum offsets between Mean Sea Level (MSL) and MLLW (Cisternelli and Gill, 2005). Then these three components are combined to compute the water level data at the location of interest.

It is nearly impossible to measure this interpolation uncertainty directly. The interpolation uncertainty can be determined by comparing the interpolated water level data and the observed water level data.

Discrete tidal zoning: In the case of a survey area covered by discrete tidal zoning schemes, because the water level data used to interpolate or extrapolate is the observed data rather than the data predicted using harmonic constants, the uncertainty sources will not include harmonic constant uncertainty and Laplace Equation interpolation uncertainty. Instead, an uncertainty in the application of tidal or water level zoning will be included in the uncertainty sources (Gibson and Gill, 1999). The water level uncertainty sources for the direct tidal zoning case include water level observation uncertainty, uncertainty in computation of tidal datum for the adjustment to a 19-year NTDE from short-term stations, and uncertainty in the application of tidal or water level zoning.

The analyses on water level observation uncertainty and tidal datum uncertainty are the same as those for TCARI. Like Laplace Equation interpolation uncertainty, uncertainty in the application of tidal or water level zoning can also be estimated by comparing the interpolated data and the observed data. A typical uncertainty value associated with tidal zoning is 0.2 meter at 95% confidence level (personal communication, Stephen Gill, NOAA/NOS/CO-OPS, 2012). However, in areas with complex and ill-defined tide characteristics or in areas where meteorology is the major tide forcing, the tidal zoning uncertainty may dominate the uncertainty in water level data, and its value may exceed 0.2 meter at 95% confidence level.

3.1.4 Human Compilation Uncertainty

The accuracy of human compilation depends on image quality (such as resolution, contrast and brightness), the compiler's knowledge about the survey area, the compiler's shoreline compilation experience, and the complexity of the survey area. These factors cannot be quantified simply and thus it is difficult to build an appropriate mathematical model to describe human compilation uncertainty. Therefore, in this thesis the shoreline compilation results from different compilers are analyzed to obtain an approximate human compilation uncertainty value.

The steps for human compilation uncertainty analysis are as follows:

- (1) Ask compilers with different experience to interpret a MHW or MLLW shoreline;
- (2) Create a reference shoreline using USGS's Digital Shoreline Analysis System (DSAS) utility (Thieler *et al.*, 2009);

- (3) Generate shoreline transects perpendicular to the reference shoreline at a given interval;
- (4) In each transect, calculate the distances between the compiled shorelines and the reference shoreline;
- (5) Obtain the location of the “true” shoreline in each transect by calculating the mean of the distances calculated in the last step (here the mean of all the compilers’ shorelines is treated as the “true” shoreline);
- (6) In each transect, calculate the distances between the compiled shorelines and the “true” shoreline;
- (7) Accumulate statistics of the horizontal offsets (the RMS of the horizontal offsets) and get the final human compilation uncertainty.

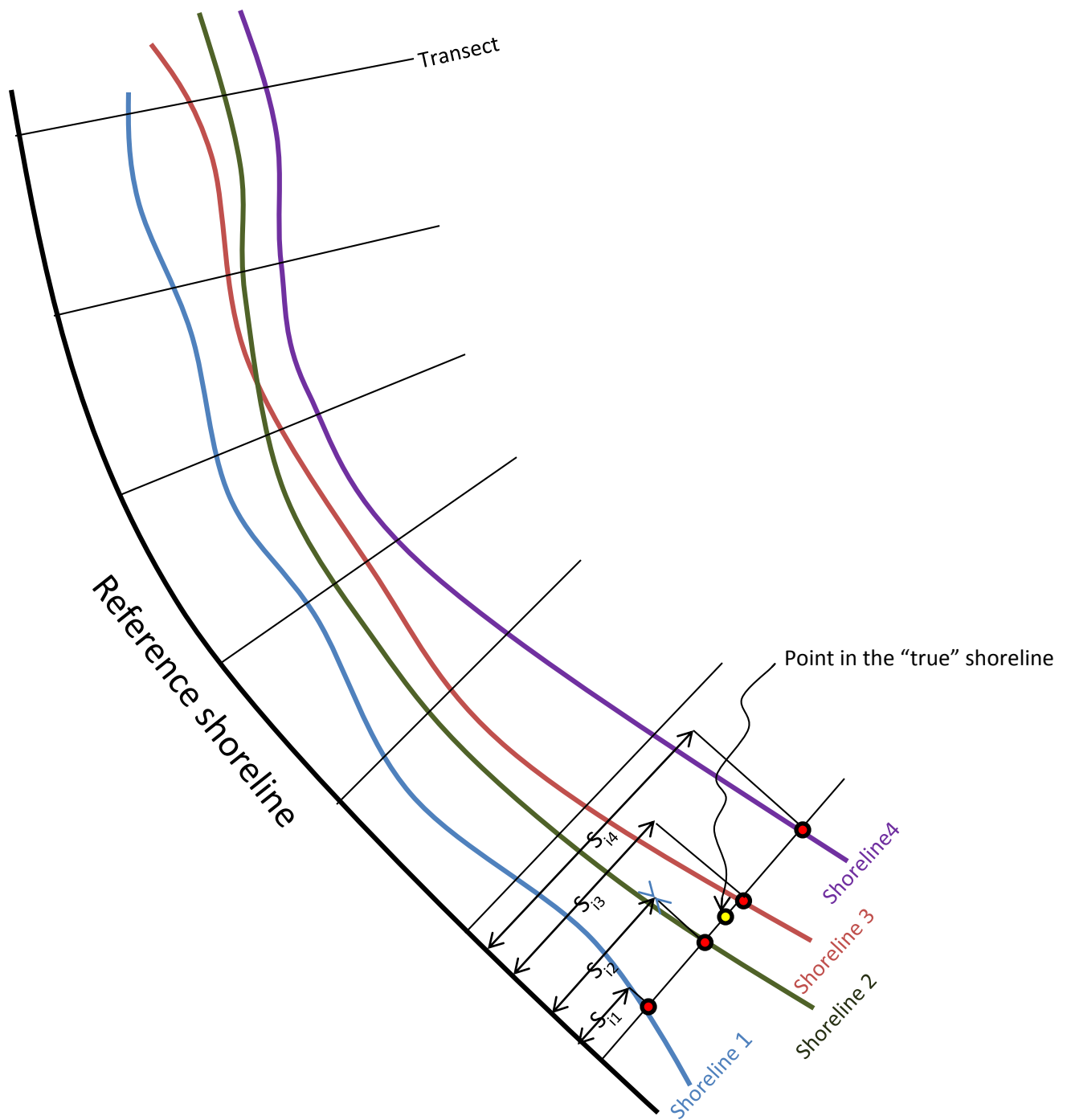


Figure 3.7 Human compilation uncertainty analysis

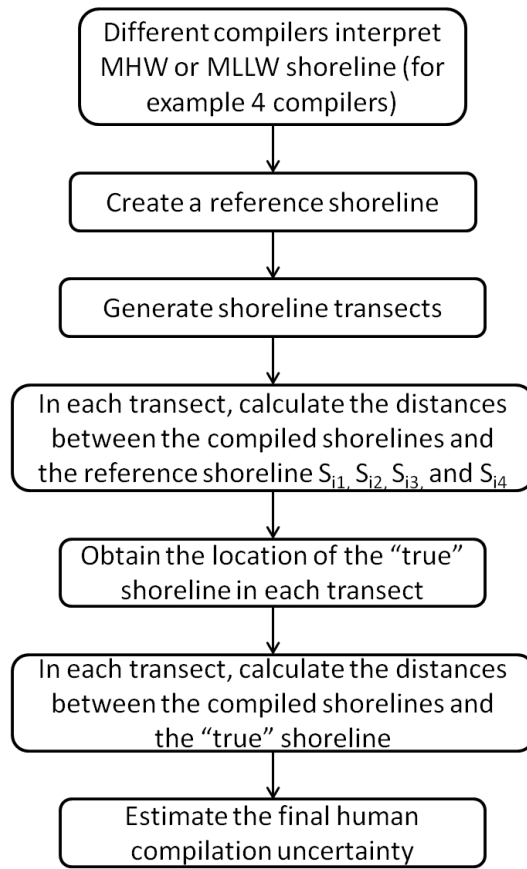


Figure 3.8 Flowchart of human compilation uncertainty computation

3.1.5 Total Propagated Uncertainty

For the above uncertainty components, exterior orientation element uncertainty and human compilation uncertainty are horizontal, while offset between MHW or MLLW datum and observed water level and uncertainty in water level data are vertical. The vertical uncertainty components need to be converted to the horizontal uncertainty components using the beach slope before calculating the total uncertainty,

$$u_h = \frac{u_v}{\tan\theta} \quad (3.10)$$

where u_v is a vertical uncertainty component, u_h is the horizontal uncertainty caused by the vertical uncertainty component, and θ is the beach slope. The beach slope can be extracted from a Digital Elevation Model (DEM), for example, using “Spatial Analyst->Slope” function in ArcGIS. A vertical uncertainty will cause a greater horizontal uncertainty in a gentle area than that in a steep area.

Each uncertainty component is assumed to be independent of the others, and so the total standard uncertainty (at 68% confidence level) and the uncertainty at 95% confidence level are computed using

$$u = S + t_{68,v}R \quad (3.11)$$

$$U_{95} = S + t_{95,v}R \quad (3.12)$$

where u is the standard uncertainty (at 68% confidence level); U_{95} is the uncertainty at 95% confidence level; $t_{68,v}$ is the Student’s t (or coverage factor) for 68% confidence level and v degrees of freedom; $t_{95,v}$ is the Student’s t (or coverage factor) for 95% confidence level and v degrees of freedom; when degrees of freedom are infinite, $t_{68,v}$ and $t_{95,v}$ are 1 and 1.96 respectively; when there are fewer than 30 degrees of freedom, the sample standard deviation is smaller than the population standard deviation, so Student’s t is used to compensate for the sample standard deviation (Dieck, 2002); S is the sum of all systematic uncertainties, and R is the root sum square of all random uncertainties. Offset between MHW or MLLW datum and the observed water level and tidal datum uncertainty

(one source of uncertainty in water level data) are treated as systematic uncertainties, while the other uncertainty sources are modeled as random uncertainties (Table 3.1).

The degrees of freedom can be obtained (Dieck, 2002):

$$d.f. = v = \frac{\left[\sum_{i=1}^N (r_i)^2 + \sum_{j=1}^M (s_j/2)^2 \right]^2}{\left[\sum_{i=1}^N \frac{(r_i)^4}{v_i} + \sum_{j=1}^M \frac{(s_j/2)^4}{v_j} \right]} \quad (3.13)$$

where r_i is the i^{th} random uncertainty ($1 \leq i \leq N$, N is the number of random uncertainty components), v_i is the degrees of freedom for the i^{th} random uncertainty, s_j is the j^{th} systematic uncertainty component ($1 \leq j \leq M$, M is the number of systematic uncertainty components), v_j is the degrees of freedom for the j^{th} systematic uncertainty.

Table 3.1 Uncertainty components for tide-coordinated shoreline

| Uncertainty component | | | Uncertainty type |
|---|-----------------------|--|------------------|
| Exterior orientation element uncertainty | | | Random |
| Offset between MHW or MLLW Datum and Observed Water Level | | | Systematic |
| Uncertainty in water level data | TCARI | Water level observation uncertainty | Random |
| | | Harmonic constant uncertainty | Random |
| | | Tidal datum uncertainty | Systematic |
| | | Laplace Equation interpolation uncertainty | Random |
| | Discrete tidal zoning | Water level observation uncertainty | Random |
| | | Tidal datum uncertainty | Systematic |
| | | Tidal zoning uncertainty | Random |

| | |
|-------------------------------|--------|
| Human compilation uncertainty | Random |
|-------------------------------|--------|

Besides the uncertainty models ((3.11) and (3.12)), there are some other uncertainty models combining systematic uncertainties and random uncertainties (Dieck, 2002). The reason why (3.11) and (3.12) are adopted in this thesis is that NOAA is using these two models in other applications, such as computing uncertainty in water level data, and it is better to keep the uncertainty models consistent in all of NOAA's uncertainty computations. In addition, these two models are conservative in estimating total uncertainty.

The two formulas ((3.11) and (3.12)) can be expressed using each uncertainty source as follows:

For TCARI:

$$u = (u_{of} + u_d) + t_{68,v} \sqrt{u_e^2 + u_{ob}^2 + u_{ha}^2 + u_i^2 + u_{hu}^2} \quad (3.14)$$

$$U_{95} = (u_{of} + u_d) + t_{95,v} * \sqrt{u_e^2 + u_{ob}^2 + u_{ha}^2 + u_i^2 + u_{hu}^2} \quad (3.15)$$

For discrete tidal zoning:

$$u = (u_{of} + u_d) + t_{68,v} \sqrt{u_e^2 + u_{ob}^2 + u_z^2 + u_{hu}^2} \quad (3.16)$$

$$U_{95} = (u_{of} + u_d) + t_{95,v} \sqrt{u_e^2 + u_{ob}^2 + u_z^2 + u_{hu}^2} \quad (3.17)$$

where u_e is exterior orientation element uncertainty; u_{of} is offset between MHW or MLLW datum and observed water level; u_{ob} , u_{ha} , u_d , u_i and u_z are water level observation uncertainty, harmonic constant uncertainty, tidal datum uncertainty, Laplace

Equation interpolation uncertainty and tidal zoning uncertainty respectively; and u_{hu} is human compilation uncertainty.

3.2 Shoreline Uncertainty based on Non-Tide-Coordinated Imagery

When shoreline is compiled on non-tide-coordinated imagery, only three main uncertainty sources contribute to the total uncertainty: (1) exterior orientation element uncertainty; (2) uncertainty in water level data; and (3) human compilation uncertainty. The offset between MHW and the observed water level is compensated for in compilation; it is not an uncertainty component for non-tide-coordinated shoreline. One difference from the tide-coordinated case is that the photogrammetrist is compiling an elevation contour, as opposed to a planimetric feature (the land-water interface). Hence, the human compilation uncertainty is not the same in the two cases.

3.2.1 Exterior Orientation Element Uncertainty

The exterior orientation element uncertainty analysis for non-tide-coordinated shoreline is the same as that for tide-coordinated shoreline.

3.2.2 Uncertainty in Water Level Data

The analysis of uncertainty in water level for non-tide-coordinated shoreline is the same as that for tide-coordinated shoreline.

3.2.3 Human Compilation Uncertainty

Because the compilation from the non-tide-coordinated imagery is primarily done based on elevation information, the human compilation uncertainty for non-tide-coordinated

shoreline is analyzed in elevation. The first six steps in human compilation uncertainty analysis for tide-coordinated shoreline can be used to calculate the horizontal human compilation uncertainty for non-tide-coordinated shoreline in each transect. The relationship between the horizontal human compilation uncertainties and the slopes is linearly fitted using the least square method. The slope of the fitted straight line is the vertical human compilation uncertainty.

3.2.4 Total Propagated Uncertainty

For the three uncertainty components for non-tide-coordinated shoreline, exterior orientation element uncertainty is horizontal, while uncertainty in water level data and human compilation uncertainty are vertical. The vertical uncertainty components need to be converted to the horizontal uncertainty components using the formula (3.10) before calculating the total uncertainty.

Table 3.2 Uncertainty components for non-tide-coordinated shoreline

| Uncertainty component | | | Uncertainty type |
|--|-----------------------|--|------------------|
| Exterior orientation element uncertainty | | | Random |
| Uncertainty in water level data | TCARI | Water level observation uncertainty | Random |
| | | Harmonic constant uncertainty | Random |
| | | Tidal datum uncertainty | Systematic |
| | | Laplace Equation interpolation uncertainty | Random |
| | Discrete tidal zoning | Water level observation uncertainty | Random |
| | | Tidal datum uncertainty | Systematic |
| | | Tidal zoning uncertainty | Random |

| | |
|-------------------------------|--------|
| Human compilation uncertainty | Random |
|-------------------------------|--------|

The total standard uncertainty (at 68% confidence level) and the uncertainty at the 95% confidence level can be expressed using each uncertainty source as follows:

For TCARI:

$$u = u_d + t_{68,v} \sqrt{u_e^2 + u_{ob}^2 + u_{ha}^2 + u_i^2 + u_{hu}^2} \quad (3.18)$$

$$U_{95} = u_d + t_{95,v} \sqrt{u_e^2 + u_{ob}^2 + u_{ha}^2 + u_i^2 + u_{hu}^2} \quad (3.19)$$

For discrete tidal zoning:

$$u = u_d + t_{68,v} \sqrt{u_e^2 + u_{ob}^2 + u_z^2 + u_{hu}^2} \quad (3.20)$$

$$U_{95} = u_d + t_{95,v} \sqrt{u_e^2 + u_{ob}^2 + u_z^2 + u_{hu}^2} \quad (3.21)$$

CHAPTER 4 – EXPERIMENTAL RESULT

4.1 Shoreline Uncertainty based on Tide-Coordinated Imagery

4.1.1 Exterior Orientation Element Uncertainty

The DSS camera parameters used in this study for estimating the point positioning uncertainty caused by the exterior orientation element uncertainties include (Applanix, 2014): the flying height over ground, 3048 m; camera focal length, 60.265 mm; pixel size on CCD chip, 6.8 μm ; CCD length in the along-track direction, 5408 pixels; CCD length in the across-track direction, 7212 pixels, and exterior orientation elements of each image and their standard uncertainties.

Although the computation result will be more accurate with an increase in Monte Carlo simulation trials, processing time should be taken into account. The first image pair was tested to determine the number of simulation trials for each image point (100 equally spaced image points were used from the left image). Figure 4.1 illustrates the relationships between the number of the simulation trials and $X/Y/Z$ uncertainty caused by exterior orientation element uncertainties for this image pair. When the number of the simulation

trials was greater than 2000, the changes of X , Y and Z uncertainties with the change of the number of the simulation trials were less than 0.005m, 0.005m and 0.02 m respectively. Therefore, 2000 simulation trials were implemented for each image point, and in this case the computation time for the first image pair was about 4 seconds on a Windows PC with a 2.5 GHz processor and 6 GB of RAM.

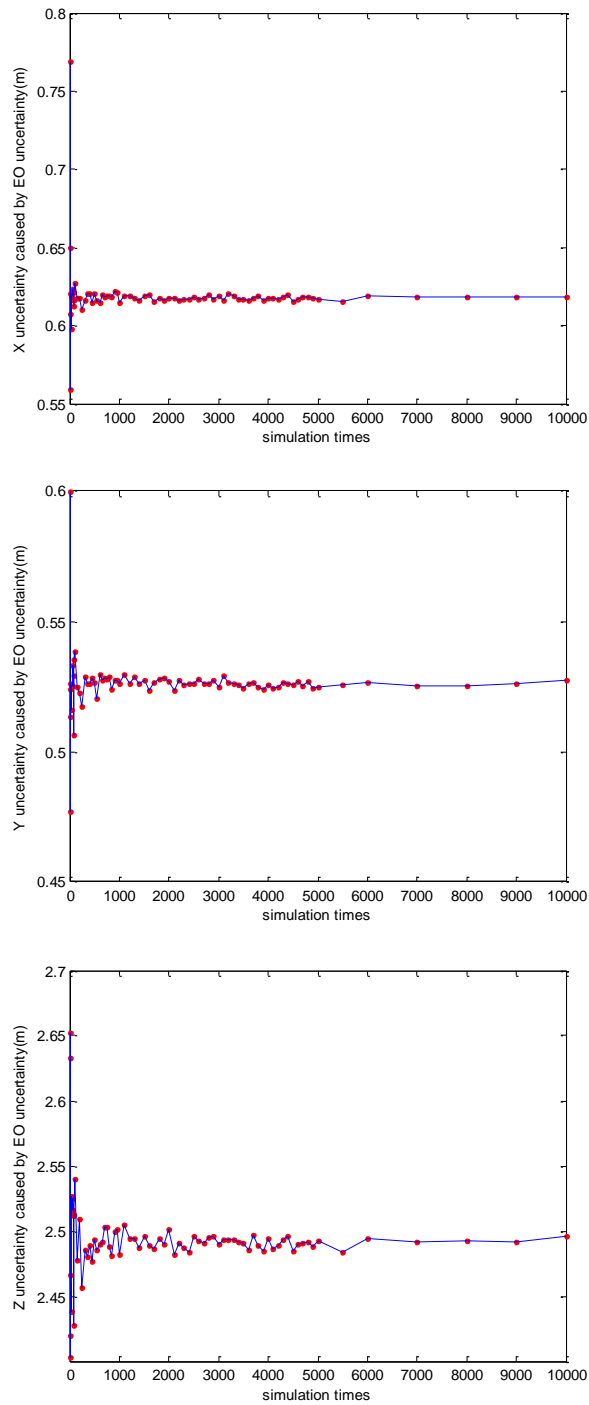


Figure 4.1 The relationships between the number of the simulation trials and X/Y/Z uncertainty caused by exterior orientation element uncertainties

For the point positioning uncertainty computation for the whole survey area, the number of simulation trials for each image point was adjusted based on the number of image pairs:

2000 divided by the number of image pairs. In this way, an increase in the number of image pairs barely increases the total computation time and, at the same time, the accuracy of the point positioning uncertainty computation for the whole survey could be ensured.

The total point positioning uncertainty computation time for this project was about 5 seconds using the same PC. The ground coordinate uncertainties caused by the exterior orientation element uncertainties are shown in Table 4.1.

Table 4.1 The uncertainty of the ground coordinates caused by the exterior orientation element uncertainties

| | |
|---------------|-------|
| X uncertainty | 0.61m |
| Y uncertainty | 0.56m |
| Z uncertainty | 2.50m |

According to the DRMS formula (3.5), for the whole survey area, the position uncertainty caused by the exterior orientation element uncertainties was 0.84m.

From the collinearity equations, it can be concluded that the point positioning uncertainty is determined mainly by the exterior orientation element uncertainties and the photographic scale at a fixed image overlap (normally the end lap and the side lap are about 60% and 30% respectively). In order to understand how each parameter influences the point positioning uncertainty, the first image pair (Table 4.2) was selected to do a sensitivity analysis.

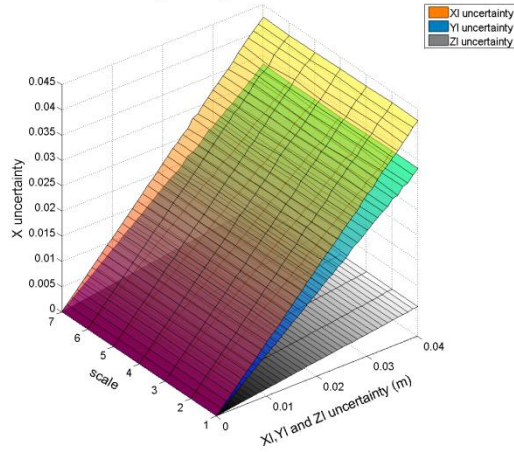
The ranges of the exterior orientation element uncertainties and the photographic scale were artificially set as follows: exterior orientation line element uncertainty [0, 0.04m];

exterior orientation angle element uncertainty $[0, 0.02^\circ]$; and photographic scale $[1:2000, 1:14000]$. In this experiment, photographic scale was changed by artificially adjusting the value of the flying height with the focal length remaining constant. At different photographic scales, the influence of each exterior orientation element uncertainty on point positioning uncertainty was analyzed. When computing the point positioning uncertainty caused by the uncertainty of one exterior orientation element, the uncertainties of the other exterior orientation elements were set to be 0. Figure 4.2 illustrates the change of the point positioning uncertainty with the change of the exterior orientation element uncertainties and the photographic scale.

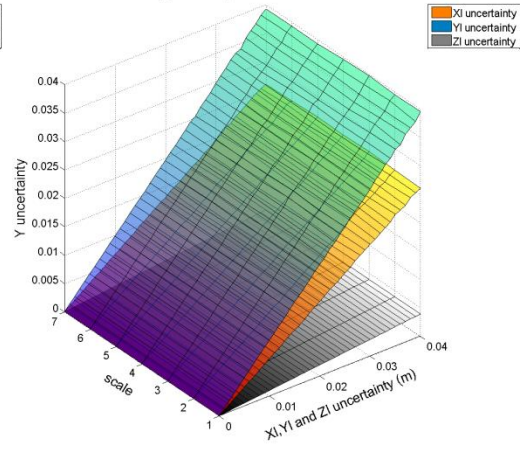
Table 4.2 The exterior orientation elements of the first image pair

| | X_L (m) | Y_L (m) | Z_L (m) | ω (degree) | φ (degree) | κ (degree) |
|---------|------------|-------------|-----------|-------------------|--------------------|-------------------|
| Image 1 | 645493.401 | 4969408.741 | 3013.527 | -3.454139 | -2.583602 | 53.705195 |
| Image 2 | 646016.418 | 4969954.652 | 3012.996 | -2.179865 | -0.140796 | 53.884717 |

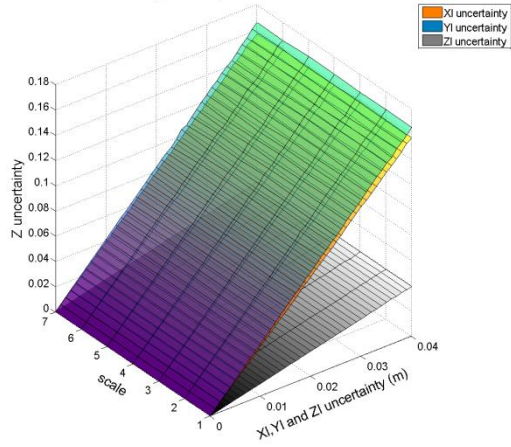
The influence of X_I , Y_I and Z_I uncertainty on the ground point coordinate X



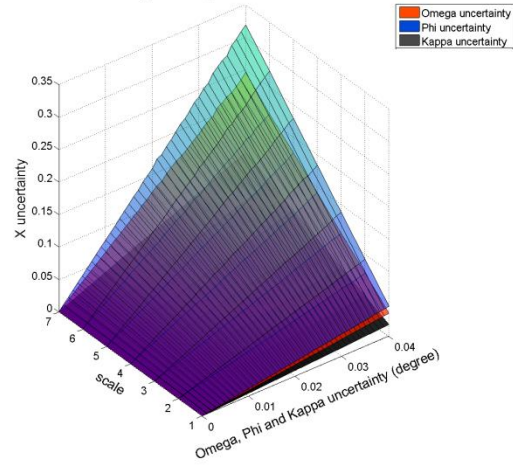
The influence of X_I , Y_I and Z_I uncertainty on the ground point coordinate Y



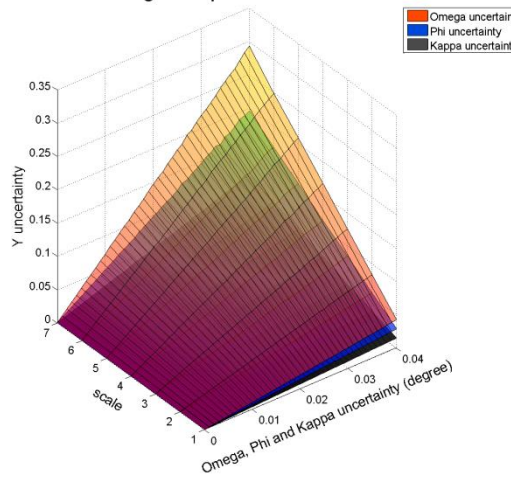
The influence of X_I , Y_I and Z_I uncertainty on the ground point coordinate Z



The influence of Ω , Φ and κ uncertainty on the ground point coordinate X



The influence of Ω , Φ and κ uncertainty on the ground point coordinate Y



The influence of Ω , Φ and κ uncertainty on the ground point coordinate Z

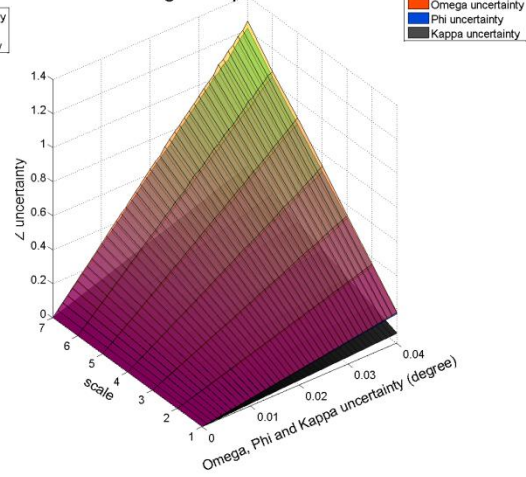


Figure 4.2 The influence of the exterior orientation element uncertainties and the photographic scale on the point positioning uncertainty (for the first image pair)

In addition, an exterior orientation element dataset of an image pair was simulated based on the first image pair (Table 4.3). The baseline length was the same as that of the first image pair, which was computed by the exterior orientation line elements of the two exposure stations, to guarantee their end laps were the same, and the flight direction was adjusted to be along the X axis. Figure 4.3 illustrates the change of the point positioning uncertainty with the change of the exterior orientation element uncertainties and the photographic scale.

Table 4.3 The exterior orientation elements of the simulated image pair

| | X_L (m) | Y_L (m) | Z_L (m) | ω (degree) | φ (degree) | κ (degree) |
|---------|------------|-------------|-----------|-------------------|--------------------|-------------------|
| Image 1 | 645493.401 | 4969408.741 | 3013.527 | -3.454139 | -2.583602 | 0 |
| Image 2 | 646249.421 | 4969408.741 | 3012.996 | -2.179865 | -0.140796 | 0 |

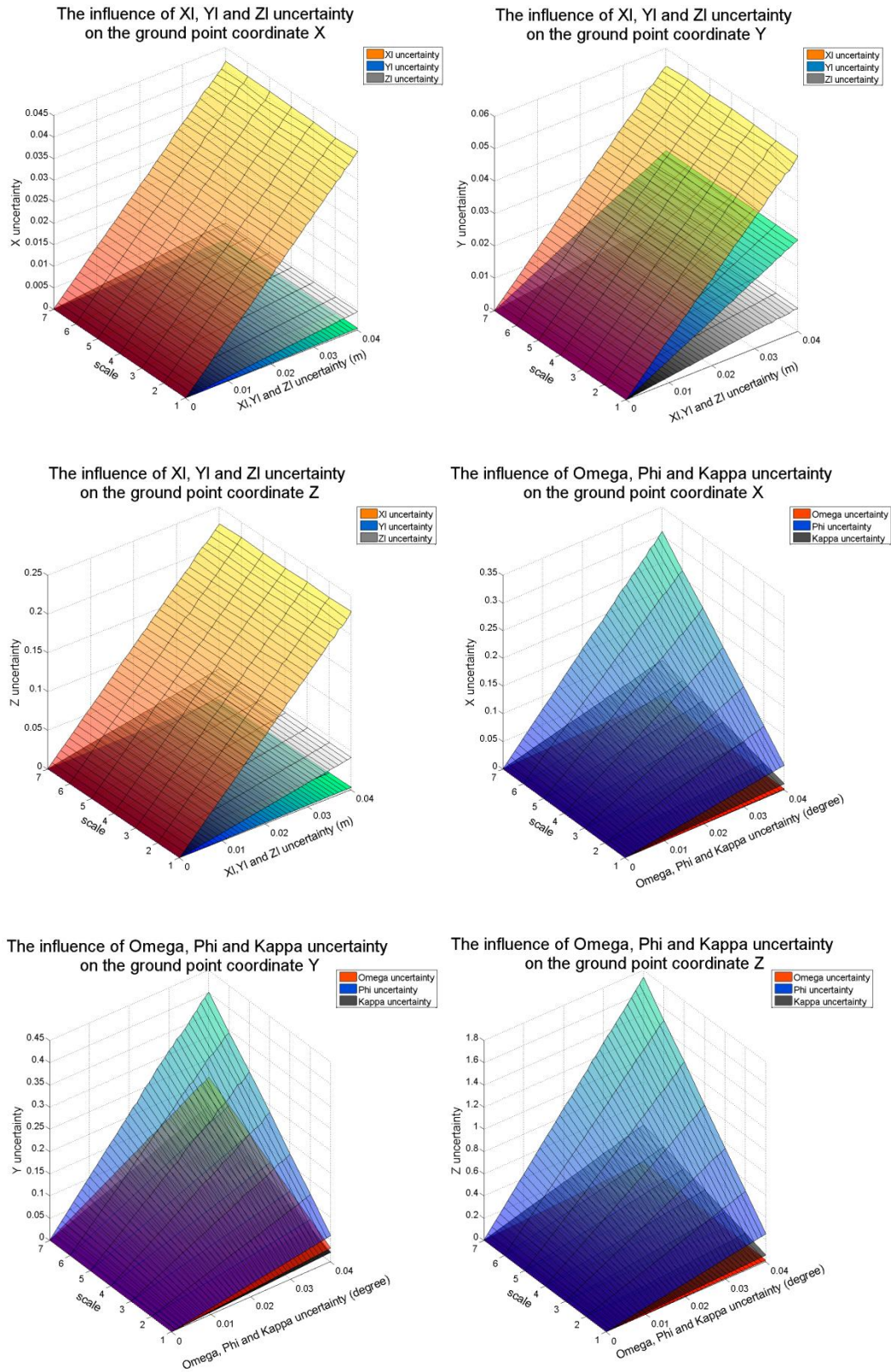


Figure 4.3 The influence of the exterior orientation element uncertainties and the photographic scale on the point positioning uncertainty (for the simulated image pair)

The sensitivity analysis results for the exterior orientation element uncertainties and the photographic scale will be discussed in the next chapter.

4.1.2 Offset between MLLW Datum and Observed Water Level

According to Table 2.2, when the two flightlines (50-001 at 14:06 and 50-002 at 14:18) were taken, the offsets between the MLLW datum and the observed water level were within the desired tolerance. The imagery taken along the two flightlines were tide-coordinated imagery, from which the MLLW lines were interpreted.

The offsets relative to the MLLW datum for both subordinate stations (Coffins Point and Birch Islands) at 14:06 and 14:18 were analyzed, and the average offset (0.30m) was treated as the offset between the MLLW datum and the observed water level for the whole survey area.

4.1.3 Uncertainty in Water Level Data

Firstly, a typical value 0.022 m (personal communication, Lijuan Huang, NOAA/NOS/CO-OPS/Hydro Planning Team, 2013) was used as the water level observation uncertainty for the survey area.

Secondly, NGS used the water level data of the EastPort station to analyze water level data of the two subordinate stations (Coffins Point and Birch Islands). The EastPort station was established in 1929, and it is a 19-year control station. Therefore, the tidal datum uncertainty for Eastport was assumed to be zero (NOAA, 2010).

Thirdly, the uncertainty in the application of tidal or water level zoning was analyzed by comparing the water level data from the Tidal Analysis Report and the prediction based on

harmonic constituents, because the harmonic constituents account for more than 99% of the total water level energy in this region and the predicted data based on harmonic constituents can be used as alternative observed data to calculate the tidal zoning uncertainty (personal communication, Lijuan Huang, NOAA/NOS/CO-OPS/Hydro Planning Team, 2013). CO-OPS provided the predicted data based on harmonic constituents for Coffins Point and the predicted data based on four time and range correction parameters for Birch Islands. Therefore, the tidal data for Coffins Point was analyzed, and its uncertainty was treated as the tidal zoning uncertainty for the whole survey area. Table 4.4 represents the tidal zoning uncertainty analysis for Coffins Point. The tidal zoning uncertainty was 0.05 m.

Table 4.4 Tidal zoning uncertainty analysis for Coffins Point

| Time | Water level data relative to MLLW | | Difference (m) | RMS of differences (m) |
|-------|-----------------------------------|---|----------------|---------------------------|
| | From tide analysis report (m) | Predicted data based on harmonic constituents (m) | | |
| 13:18 | 0.59 | 0.66 | 0.07 | 0.05 |
| 13:24 | 0.58 | 0.58 | 0 | |
| 14:06 | 0.27 | 0.23 | 0.04 | |
| 14:18 | 0.27 | 0.21 | 0.06 | |

Because the sample size for tidal zoning uncertainty analysis was only four (3 degrees of freedom), the sample estimate of standard deviation can be skewed and be smaller than the population standard deviation.

4.1.4 Human Compilation Uncertainty

The shoreline compilation results from four compilers in the 2003 Fort Desoto, Florida project (Parrish *et al.*, 2005) were applied to analyze the tide-coordinated human compilation uncertainty due to lack of the tide-coordinated compilation results from different compilers in the survey area (Maine).

The RMSE for each compiler can be seen to be caused by human compilation uncertainty and all the other factors. The average of the four compilers' compilation offsets against the GPS ground truth was treated as the uncertainty caused by all other factors except for the human compilation uncertainty. Table 4.5 shows the human compilation uncertainty analysis based on the four compilers' compilations.

Table 4.5 Tide-coordinated human compilation uncertainty computation

(The mean and RMSE of each compiler were obtained by comparing land/water interface and the GPS ground truth. The negative mean uncertainty means a seaward offset against the GPS ground truth)

| Shoreline | Mean (m) | RMSE (m) | $\sqrt{RMSE^2 - Average^2}$ | Human compilation uncertainty (m) (RMS of the fourth column) |
|------------|----------|----------|-----------------------------|--|
| Compiler 1 | -0.59 | 0.94 | 0.33 | 1.06 |
| Compiler 2 | -1.56 | 1.94 | 1.73 | |
| Compiler 3 | -0.39 | 0.92 | 0.27 | |
| Compiler 4 | -0.98 | 1.45 | 1.15 | |
| Average | -0.88 | | | |

The human compilation uncertainty was found to be 1.06 m. Like the tidal zoning uncertainty analysis, the sample size of the tide-coordinated human compilation uncertainty analysis was also very small (3 degrees of freedom). Therefore, the population

standard deviation of the tide-coordinated human compilation uncertainty can be greater than 1.06m. In addition, given that the coastal area in the Maine site is more complex than that in Fort Desoto and there are more types of shorelines in the Maine site, the human compilation uncertainty for the Maine site may be greater than that for Fort Desoto. Therefore, it is reasonable to suppose that 1.06m underestimated the tide-coordinated human compilation uncertainty for the Maine site.

4.1.5 Total Propagated Uncertainty

Among the above four uncertainty components, the offset between the MLLW datum and the observed water level and the uncertainty in water level data are vertical uncertainty components, while the exterior orientation uncertainty and the human compilation uncertainty are horizontal uncertainty components. All vertical uncertainty components should be converted to the horizontal uncertainty components using the beach slope before calculating the total uncertainty.

The beach slope was extracted from LiDAR data using ArcGIS. The slope raster imagery was then processed by a smoothing (low pass) filter, which calculated the average value for each 3×3 neighborhood. The high and low values within each neighborhood were averaged out, reducing the extreme values of the beach slopes (Figure 4.4).

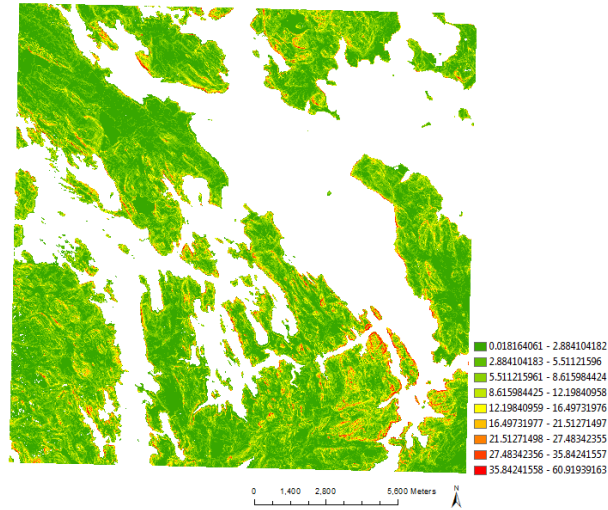


Figure 4.4 Filtered slope raster imagery

After obtaining the beach slope, the reference shorelines were firstly created, and then transects at the interval of 2m along shorelines were generated using DSAS. On each transect, the vertical uncertainty components were converted to horizontal uncertainty components.

The degrees of freedom for the tidal zoning uncertainty and the human compilation uncertainty were 3, and the degrees of freedom for all the other uncertainty components were assumed to be infinite. The degrees of freedom for the total uncertainty were computed using the value of each uncertainty component and their degrees of freedom according to (3.13), then the total standard uncertainty and the uncertainty at the 95% confidence level were estimated according to (3.16) and (3.17). The RMSs of the uncertainties on all the transects were the total uncertainties for the whole survey area: 3.28m total standard uncertainty and 4.77m uncertainty at the 95% confidence level.

4.2 Shoreline Uncertainty based on Non-Tide-Coordinated Imagery

4.2.1 Exterior Orientation Element Uncertainty

The point positioning uncertainty caused by the exterior orientation element uncertainties for non-tide-coordinated shoreline is the same as that for tide-coordinated shoreline.

4.2.2 Uncertainty in Water Level Data

The value of the uncertainty in water level data for non-tide-coordinated shoreline is the same as that for tide-coordinated shoreline.

4.2.3 Human Compilation Uncertainty

Nine compilers with different experience levels compiled the MHW lines from non-tide-coordinated imagery in the two regions selected from the survey area (8 degrees of freedom), and the compilation results were analyzed to determine the non-tide-coordinated human compilation uncertainty.

Two reference shorelines were first created, and then shoreline transects were generated perpendicular to the reference shorelines at 10 m spacing (Figure 4.5). The average of the compiled shorelines was treated as the shorelines without human compilation uncertainty, and then the RMS of all the compilers' uncertainties was computed in each transect as the human compilation uncertainty of this transect.



Figure 4.5 The reference shorelines (red lines) and transects (blue lines). Different colors in transects represent the degree of the maximum difference of the compilation results from the compilers.

Combined with the slope information along the two shorelines, the planimetric human compilation uncertainty was converted to uncertainty in elevation. Figure 4.6 illustrates the relationship between the slope and the planimetric human compilation uncertainty. From the distribution of the points, it can be seen that the horizontal human compilation uncertainty from non-tide-coordinated imagery depends on the beach slope, because compilers compile the shoreline based on the elevation information. When the vertical human compilation uncertainty is fixed, the horizontal human compilation uncertainty will change with the beach slope.

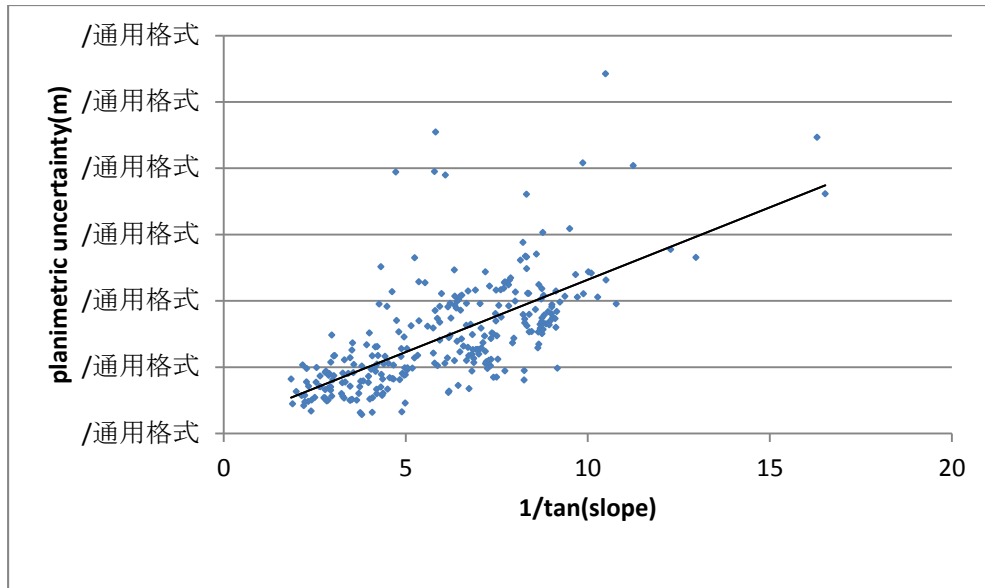


Figure 4.6 The relationship between the slope and the planimetric human compilation uncertainty

The black line is the least-square fitted straight line based on the data of planimetric human compilation uncertainty and the slope. The slope of this fitted straight line, 0.44 m, was used as the elevation uncertainty corresponding to this level of planimetric compilation uncertainty.

4.2.4 Total Propagated Uncertainty

Among the above three uncertainty components, the uncertainty in water level data and the human compilation uncertainty are vertical uncertainty components, while the exterior orientation uncertainty is a horizontal uncertainty component.

On each transect, the vertical uncertainty components were converted to horizontal uncertainty components. Here, the degrees of freedom for the tidal zoning uncertainty and the human compilation uncertainty were 3 and 8 respectively, and the degrees of freedom for all the other uncertainty components were assumed to be infinite. The degrees of

freedom for the total uncertainty were computed using the value of each uncertainty component and their degrees of freedom according to (3.13), then the total standard uncertainty and the uncertainty at the 95% confidence level were computed according to (3.20) and (3.21). The RMSs of the uncertainties on all the transects were the total uncertainties for the whole survey area: the total standard uncertainty was 3.15m and the uncertainty at the 95% confidence level was 6.73m.

The boundaries for the standard uncertainty and the uncertainty at the 95% confidence level are shown on the imagery (Figure 4.7).

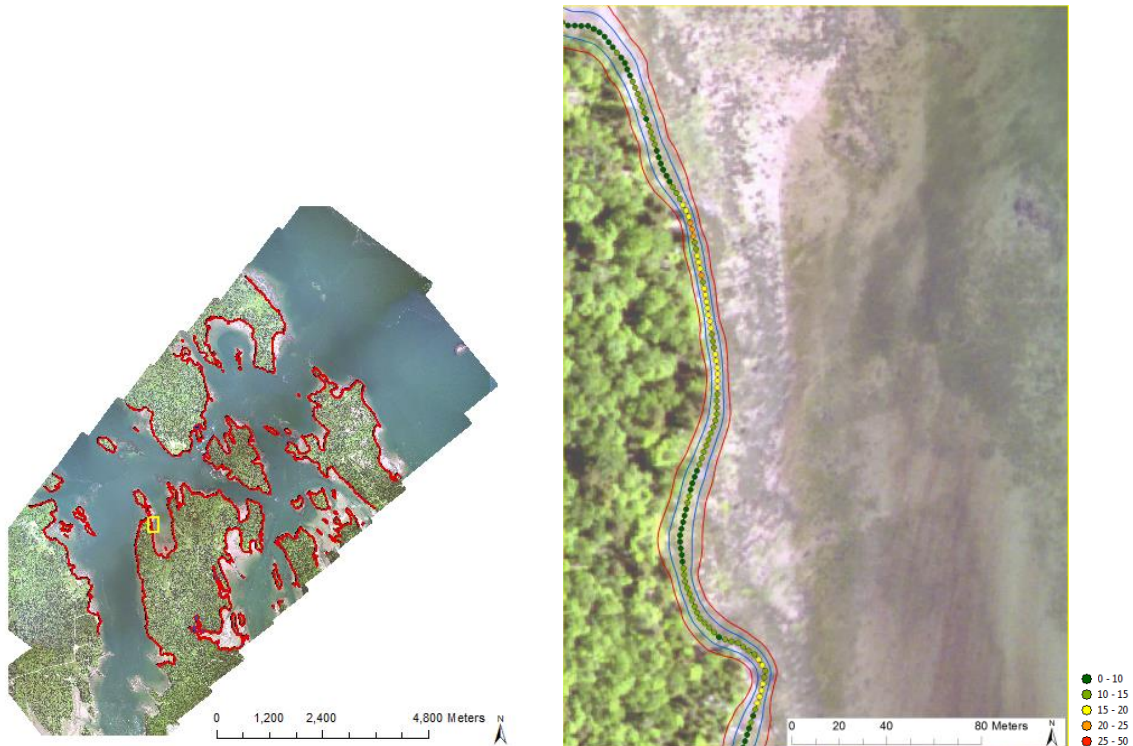


Figure 4.7 The uncertainty boundaries. The blue lines and the red lines represent the standard uncertainty and the uncertainty at the 95% confidence level respectively. The black lines are the MHW shoreline. (Left) the imagery for the whole survey area. (Right) the enlarged imagery for the yellow box in the left imagery; the points with different colors represent the slope in degrees.

From Figure 4.7 (right), it can be seen that in a region with gentle slope the uncertainty is greater than that in a steep region. It can be concluded slope is an important factor which affects the shoreline uncertainty.

CHAPTER 5 – DISCUSSION

5.1 Exterior Orientation Element Uncertainty

In the experiment, the simulation times of each pair of corresponding image points were dynamically adjusted based on the number of the image pairs (2000 divided by the number of the image pairs), and the experiment result showed that the computation time and the accuracy were both acceptable.

The sensitivity analysis of exterior orientation element uncertainties and photographic scale (Figure 4.2 and Figure 4.3) led to the following conclusions:

- (1) The point positioning uncertainty increases linearly with the increase of the exterior orientation element uncertainties.
- (2) The point positioning uncertainty caused by the exterior orientation angle element uncertainties ($\sigma_\omega, \sigma_\varphi, \sigma_\kappa$) is affected linearly by the photographic scale. The smaller the scale is, the higher the point positioning uncertainty and the greater the change of the point positioning uncertainty with the change of the exterior orientation angle element uncertainties. On the other hand, the photographic scale has negligible impact on the point positioning uncertainty caused by the exterior orientation line element uncertainties ($\sigma_{X_L}, \sigma_{Y_L}, \sigma_{Z_L}$).
- (3) The uncertainties of X_L and φ mainly affect the accuracy of the ground point coordinate X , and the uncertainties of Y_L and ω mainly affect the accuracy of the

ground point coordinate Y . However, it is important to note that these observations depend on the orientation of the flight lines with respect to true north (or the axes of the mapping frame). If the flight direction is closer to the X axis (Y axis), the uncertainties of X_L and φ (Y_L and ω) have greater influence on the point positioning accuracy.

5.2 Tidal Zoning Uncertainty

The water level data for Coffins Point at the only four different times (Table 4.4) was applied to analyze the tidal zoning uncertainty for the survey area. The sample size is so small that the tidal zoning uncertainty value from this analysis may have underestimated the actual tidal zoning uncertainty. According to the values of the Student's t for 4 and infinite sample sizes at 68% confidence level, it would be expected that the value of the actual tidal zoning uncertainty is ~ 1.2 times that of the tidal zoning uncertainty estimated by the 4 samples.

5.3 Human Compilation Uncertainty

The human compilation uncertainty was estimated by analyzing compilation results from different compilers. The estimated values for the two cases (tide-coordinated and non-tide-coordinated) cannot be easily applied to any area or any set of compilers, and they should be adjusted based on different conditions, such as compiler's experience, image quality and complexity of coastal region.

The compilation results from four compilers in Fort Desoto were applied to estimate the tide-coordinated human compilation uncertainty for the Maine site. However, the topography of the Maine site is more complex than that of Fort Desoto. Therefore, the human compilation uncertainty for Fort Desoto may have underestimated that for Maine.

In addition, the small sample sizes for the tide-coordinated and non-tide-coordinated human compilation uncertainty analysis may have resulted in the sample human compilation uncertainties being less than the population human compilation uncertainties.

According to the values of the Student's *t* for 4, 9 and infinite sample sizes at 68% confidence level, it would be expected that the value of the actual tide-coordinated human compilation uncertainty for the Maine site is greater than ~1.2 times that of the tide-coordinated human compilation uncertainty estimated by the 4 Fort Desoto compilation samples, and the value of the actual non-tide-coordinated human compilation uncertainty is ~1.06 times that of the non-tide-coordinated human compilation uncertainty estimated by the 9 Maine compilation samples.

5.4 Comparison of Tide-Coordinated and Non-Tide-Coordinated Uncertainties

Table 5.1 provides the planimetric values of each uncertainty component and the total uncertainties for this shoreline survey.

From this table, it can be seen that for tide-coordinated compilation the offset between MHW/MLLW and observed water level has the main impact on the total uncertainty, followed by human compilation uncertainty, exterior orientation element uncertainty, and then uncertainty in water level data. For non-tide-coordinated compilation, the order is

human compilation uncertainty, exterior orientation element uncertainty, and then uncertainty in water level data. In addition, the non-tide-coordinated human compilation uncertainty is greater than the tide-coordinated one. Comparing the total uncertainties for the two cases, they are not very different from each other. This indicates that it may not be necessary to require a survey to be tide-coordinated. However, the shoreline TPU would need to be computed for many survey sites to determine if this is true in general, or only for this particular survey.

Table 5.1 The planimetric values (in meters) of each uncertainty component and the total uncertainties for the survey area (The tidal zoning uncertainty and the human compilation uncertainty were computed using their sample uncertainty values multiplied by their corresponding Student's t)

| | Exterior orientation element uncertainty | The offset between MHW or MLLW datum and observed water level | Uncertainty in water level data | | | Human compilation uncertainty | Total uncertainty | |
|----------------------|--|---|---------------------------------|-------|--------|-------------------------------|-------------------|--------|
| | | | Observation | Datum | Zoning | | Std | 95% CI |
| Tide-coordinated | 0.84 | 1.96 | 0.15 | 0 | 0.39 | 1.26 | 3.28 | 4.77 |
| Non-tide-coordinated | 0.84 | 0 | 0.15 | 0 | 0.39 | 3.03 | 3.15 | 6.73 |

5.5 Relationship between Uncertainty and Slope

For the study area, the ranges of the standard uncertainties for tide-coordinated and non-tide-coordinated compilation along the different transects are [1.72m, 31.20m] and [0.93m, 40.78m] (Figure 5.1). The variability in the uncertainty is primarily attributable to slope variation (Figure 5.2). In areas with small slope, the uncertainty is higher. The upper limits of these TPU ranges are quite large. However, they are realistic, since in some sections of the study area the beach slope is extremely small, such as 0.66° . These upper limits of the uncertainty ranges should not be taken as a reflection of the standard uncertainty for the

study area as a whole, but it is important to note that the uncertainty in a few localized areas can be significantly greater than the standard shoreline uncertainty for the survey area.

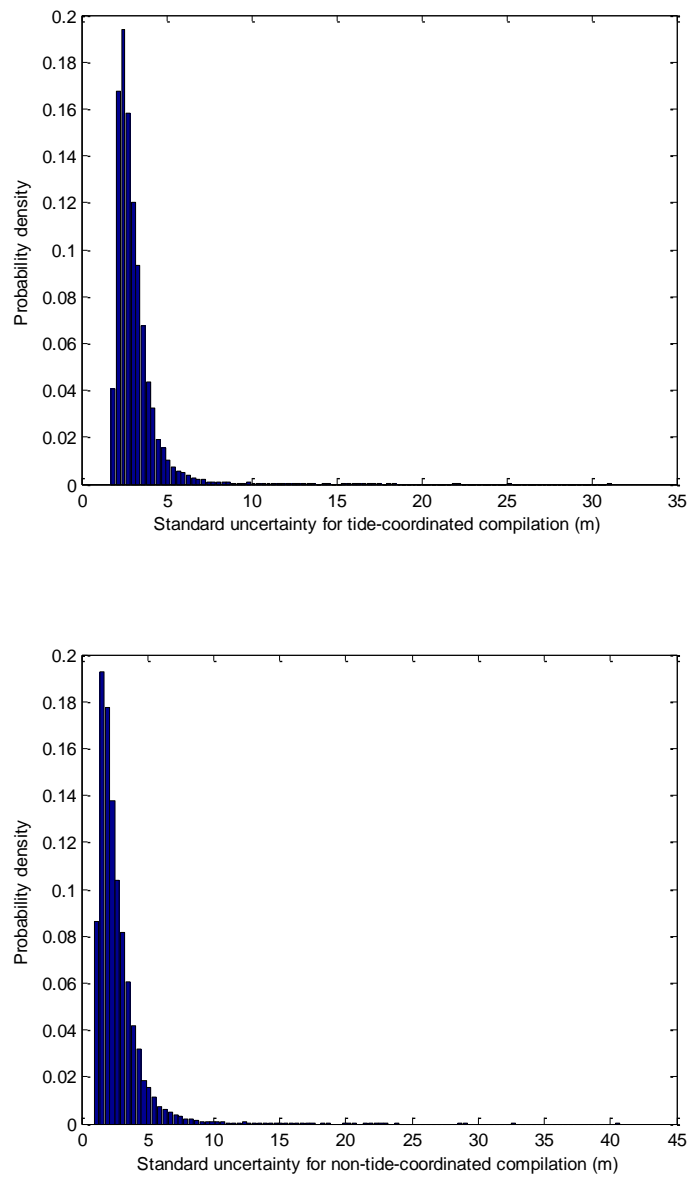


Figure 5.1 Distribution of standard uncertainties for tide-coordinated and non-tide-coordinated compilation

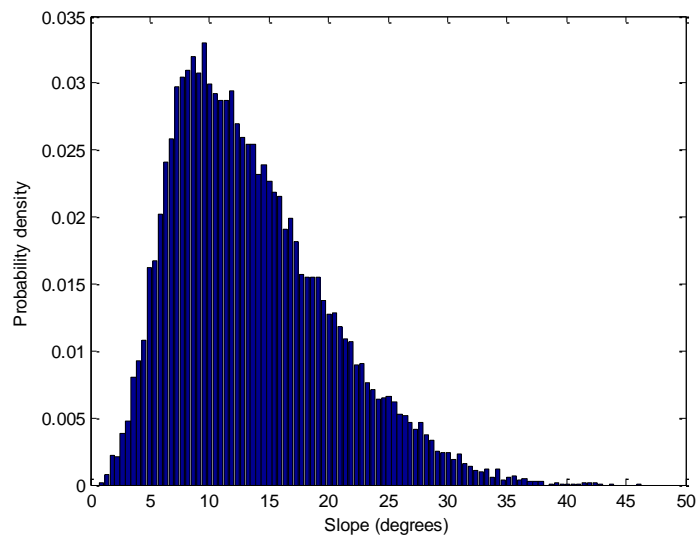


Figure 5.2 Distribution of slopes

CHAPTER 6 – CONCLUSIONS AND RECOMMENDATIONS FOR FUTURE WORK

The photogrammetric method for shoreline mapping has many advantages: maturity, capability of mapping large areas with great detail quickly, access to certain areas where field surveys are infeasible, and good accuracy for man-made/built-up shorelines. Therefore, it has been the main shoreline mapping method used by NGS since 1927. Compared with the development of this technique, the statistical method of estimating the photogrammetry-derived shoreline uncertainty has lagged behind. This thesis therefore proposes a TPU model in order to generate metadata containing accuracy for the national shoreline, which will make the shoreline product more useful. The uncertainty boundaries generated based on the uncertainty values in ArcGIS enable users to understand the shoreline uncertainty visually.

In addition to providing the shoreline metadata, this TPU model can also be used before a survey to judge whether a given accuracy requirement can be met based on the accuracy of the integrated GPS/IMU system, photographic scale, predicted water level, human compilation uncertainty and other factors. This analysis, if conducted in advance of a survey, can be used to modify acquisition procedures to maximize efficiency and ensure adherence to applicable specifications.

Through the uncertainty analysis for the study area (northeast coast of Maine), it can be seen that the total uncertainties for tide-coordinated shoreline compilation and non-tide-coordinated shoreline compilation are similar. This suggests that, if the pre-survey uncertainty estimation meets the accuracy requirement, survey time can be determined based on weather conditions, and does not necessarily have to be tide-coordinated.

In addition, from the experiment results it can be concluded that the offset between MHW/MLLW datum and observed water level is the most important uncertainty component for tide-coordinated shoreline compilation, and for non-tide-coordinated shoreline compilation human compilation uncertainty is most significant. In order to efficiently reduce the total uncertainty, for tide-coordinated shoreline compilation aerial imagery should be taken at the time when predicted water level is closer to MHW/MLLW datum, and for non-tide-coordinated shoreline compilation, the level of the compiler's experience is critical.

However, there are still several topics which need to be examined in future research, including:

- (1) The human compilation uncertainty was estimated by analyzing compilation results from different compilers. The estimated values for the two cases (tide-coordinated and non-tide-coordinated) cannot be easily applied to another area or set of compilers, and they should be adjusted based on different conditions. In fact, this uncertainty should be estimated as a function of additional variables, including the compiler's experience, complexity of the coast, and image quality. Modeling human compilation uncertainty should be one of the

important goals for future work, including how to judge the compiler's experience, complexity of the coast, and image quality, and how to weigh these factors in one model. From the model, we would like to determine how each factor influences the human compilation uncertainty and the range of this uncertainty.

- (2) This TPU model should be tested in different sites. This would enable analysis of how each uncertainty component and the total uncertainty change in different conditions.
- (3) There are several techniques for shoreline mapping. Some of them are being used by NGS, and some of them are being explored. It is necessary to compare the uncertainties of different techniques. A comprehensive analysis of these techniques should be performed, including uncertainty, constraints (such as that a photogrammetric shoreline survey cannot be conducted at night), and cost both in terms of time and money. This would be useful in choosing an appropriate technique for a specific shoreline mapping project.

LIST OF REFERENCES

- Alfugura, A., L. Billa, and B. Pradhan, 2011. Semi-automated procedures for shoreline extraction using single RADARSAT-1 SAR image. *Estuarine, Coastal and Shelf Science* 95(4), 395-400.
- Applanix, 2013. POSPac MMS.
<http://www.applanix.com/products/airborne/pospacmms.html>. (accessed October 28, 2013).
- Applanix, 2014. DSS 439 Specification.
<http://www.applanix.com/media/downloads/products/specs/DSS%20439%20Specs.pdf>. (accessed April 09, 2014)
- Boak, E.H., and I.L. Turner, 2005. Shoreline definition and detection: a review. *Journal of Coastal Research* 21(4), 688-703.
- Bodnar, A.N., 1981. Estimating accuracies of tidal datums from short term observations, draft report, Tides and Water Levels Division, NOAA National Ocean Survey.
- Brennan L., 2005. An uncertainty model for the tidal constituent and residual interpolation (TCARI) method of water level correction. Master's thesis, University of New Hampshire, Durham, NH.
- Brock, J.C. and S.J. Purkis, 2009. The emerging role of Lidar remote sensing in coastal research and resource management. *Journal of Coastal Research*, 53, 1–5.
- Cisternelli M. and G. Stephen, 2005. Implementation of TCARI into NOS Hydrographic Survey Operations. *U.S. Hydro*, San Diego, California, March 29-31.
- Coastal Services Center, 2013. Digital Coast, Coastal Lidar.
<https://csc.noaa.gov/digitalcoast/data/coastallidar>. (accessed July 25, 2013).

- CO-OPS, 2014. Tides&Currents: Tides/Water Levels for 8410140 Eastport, ME 2011/06/21. <http://tidesandcurrents.noaa.gov/waterlevels.html?id=8410140&units=metric&bdate=20110621&edate=20110621&timezone=GMT&datum=MLLW&interval=6&action=data>. (accessed February 28, 2014).
- Creel, L., 2003. Ripple effects: population and coastal regions. Measure communication, September 2003. Population Reference Bureau, Washington, pp 1–7.
- Crossett, K. M., T. J. Culliton, P. C. Wiley, and T. R. Goodspeed, 2004. *Population Trends Along the Coastal United States: 1980- 2008*. National Oceanic and Atmospheric Administration (NOAA), National Ocean Service. http://oceanservice.noaa.gov/programs/mb/pdfs/coastal_pop_trends_complete.pdf (accessed January 22, 2014).
- Dieck, R.H., 2002. Measurement Uncertainty: Methods and Applications, Third Edition. ISA, The Instrumentation, Systems and Automation Society, 252p.
- Filin, S., 2001. Calibration of Airborne and Spaceborne Laser Altimeters Using Natural Surfaces, Ph.D. thesis, The Ohio State University, Columbus, Ohio.
- Gibson, W.M. and S.K. Gill. 1999. Tides and Water Level Requirements for NOS Hydrographic Surveys. International Hydrographic Review, Monaco, LXXVI(2), September 1999.
- Graham, D., M. Sault, and J. Bailey, 2003. National ocean service shoreline- past, present, and future. *Journal of Coastal Research*, SI(38), 14-32.
- Grejner-Brzezinska, D.A., 1999. Direct exterior orientation of airborne imagery with GPS/INS system: Performance analysis. *Navigation*, 46(4): 261-270.
- Hutchins, P.S. and S. Oivanki, 1994. A Comparison of shoreline measurement techniques: GPS survey, air photo interpretation, and total station survey [abs]. *Journal of the Mississippi Academy of Sciences*, 39(1), 48.
- IHO (International Hydrographic Organization), 2008. *IHO Standards for Hydrographic Surveys*, 5th edition. Monaco: International Hydrographic Bureau, 36p.

- Kinexxions, 2014. The Tides at Cobscook Bay.
<http://kinexxions.blogspot.com/2012/10/the-tides-at-cobscook-bay.html> (accessed February 27, 2014).
- Leigh, G.E., T. Blackford, and etc., 2012. Scope of Work for Shoreline Mapping under the NOAA Coastal Mapping Program (14A),
http://www.ngs.noaa.gov/ContractingOpportunities/CMPsOWV14A_FINAL.pdf (accessed January 29, 2014).
- Lindenberger, J., 1989. Test results of laser profiling for topographic terrain survey.
Proceedings of the 42nd Photogrammetric Week, Stuttgart, Germany.
- Liu H.X., D. Sherman, and S. Gu, 2007. Automated Extraction of Shorelines from Airborne Light Detection and Ranging Data and Accuracy Assessment Based on Monte Carlo. *Journal of Coastal Research*, 23(6): 1359-1369.
- Manual, D.F., 2007. Digital Elevation Model Technologies and Applications: The DEM Users Manual, 2nd Edition. American Society of Photogrammetry and Remote Sensing, 655p.
- McGlone, J.C., Mikhail E.M., Bethel J., and Mullen R., 2004. Manual of Photogrammetry Fifth Edition. American Society of Photogrammetry and Remote Sensing, 1151p.
- Mikhail, E., J. Bethel, and J. McGlone, 2001. Introduction to modern photogrammetry. John Wiley & Sons, New York, 479 p.
- Mostafa M. M.R., J. Hutton, and E. Lithopoulos, 2001. Airborne Direct Georeferencing of Frame Imagery: An Error Budget. *The 3rd International Symposium on Mobile Mapping Technology*, Cairo, Egypt, January 3-5.
- NGS, 2014a. NGS Shoreline Mapping History.
http://www.ngs.noaa.gov/web/about_ ngs/history/NGSshoreline.shtml . (accessed January 23, 2014).
- NGS, 2014b. Coastal and Shoreline Change Analysis Program.
<http://www.ngs.noaa.gov/RSD/cscap.shtml> . (accessed February 24, 2014)

- NGS, 2014c. Synthetic Aperture Radar (SAR).
<http://www.ngs.noaa.gov/RESEARCH/RSD/main/sar/sar.shtml>. (accessed February 24, 2014)
- NGS, 2014d. NOAA Shoreline Data Explorer. <http://www.ngs.noaa.gov/NSDE/>
(accessed February 28, 2014).
- National Ocean Service (NOS), 2014. Transformations in Coastal Mapping: 1987- 2007.
<http://celebrating200years.noaa.gov/transformations/mapping/#map> (accessed February 4, 2014).
- NOAA, 2010. Technical considerations for use of geospatial data in sea level change mapping and assessment. Silver Spring, Maryland: National Oceanic and Atmospheric Administration, National Ocean Service, NOAA Technical Report NOS 2010-01, 130p.
- NOAA Fisheries, 2014. Greater Atlantic Region (formerly Northeast Region)
<http://www.nero.noaa.gov/stories/2013/boilingtidesnewenergysource.html>
(accessed February 27, 2014).
- Noye, B.J., 1974. Tide-well systems I: some non-linear effects of conventional tide well.
Journal of Marine Research, 32(2): 129-135.
- Office of Coast Survey, 2013a. Datums and transformations.
http://www.nauticalcharts.noaa.gov/csdl/learn_datum.html (accessed February 01 2013).
- Office of Coast Survey, 2013b. Chart 13394.
<http://www.charts.noaa.gov/OnLineViewer/13394.shtml> (accessed October 25, 2013).
- Office of Coast Survey, 2013c. Tidal corrector application (TCARI).
<http://www.nauticalcharts.noaa.gov/csdl/tcari.html> (accessed October 29, 2013).
- Office of Coast Survey, 2013d. Field Procedures Manual.
http://www.nauticalcharts.noaa.gov/hsd/fpm/FPM_2013_Final_5_3_13.pdf
(accessed October 29, 2013).

- Office of General Counsel, NOAA, 2014. Maritime Zones and Boundaries.
http://www.gc.noaa.gov/gcil_maritime.html. (accessed April 16, 2014)
- Pajak, M.J., and S.P. Leatherman, 2000. The high water line as shoreline indicator.
Journal of Coastal Research, 18(2): 329-337.
- Papadopoulos, C.E. and Yeung, H., 2001. Uncertainty estimation and Monte Carlo simulation method. *Flow Measurement and Instrument*, 12, 291–298.
- Parrish, C.E., M. Sault, S.A. White, and J. Sellars, 2005. Empirical analysis of aerial camera filters for shoreline mapping. *Proceedings of the ASPRS 2005 Annual Conference*, 7-11 March, Baltimore, MD.
- Parrish, C.E., 2011. Shoreline Uncertainty-Motivation and Research Objective. Parrish, C. 2011 CCOM Progress Report.
- Parrish, C.E., 2012. Shoreline Mapping, in *Advances in Mapping from Remote Sensor Imagery: Techniques and Applications*, CRC Press, (X. Yang and J. Li, Eds.), Taylor and Francis Group, Boca Raton, Florida, pp. 145- 168.
- Pe'eri, S., C.E. Parrish, C. Azuik, L. Alexander, and A.A. Armstrong, 2014. Satellite Remote Sensing as a Reconnaissance Tool for Assessing Nautical Chart Adequacy and Completeness, *Marine Geodesy*. (Submitted) Royal Swedish Academy of Sciences, 2012. Sea Level Changes Report.
http://www.kva.se/Documents/Vetenskap_samhället/Energi/Utskottet/2012/rapport_energi_havsvattenstand_eng_2012.pdf (accessed January 22, 2014).
- Philpot, W.D., 2012. Photogrammetry, Remote Sensing Fundamentals.
http://ceeserver.cce.cornell.edu/wdp2/cee6100/6100_monograph/mono_07_F12_photogrammetry.pdf (accessed February 22, 2014).
- Porter, D. L. and H. H. Shih, 1996. Investigations of temperature effects on NOAA's next generation water level measurement system. *Journal of Atmospheric and Oceanic Technology*, 13(3):714-725.
- Royal Swedish Academy of Sciences, 2012. Sea Level Changes Report.
http://www.kva.se/Documents/Vetenskap_samhället/Energi/Utskottet/2012/rapport_energi_havsvattenstand_eng_2012.pdf (accessed January 22, 2014).

- Shalowitz, A.L., 1964. Shore and sea boundaries. U.S. Department of Commerce, U.S. Coast and Geodetic Survey.
- Shih, H.H., D.H. Deitemyer and M.W. Allen, (1984). Field Evaluation of a New Tide Gage Stilling Well Design. *Proc. 3rd International Offshore Mechanics and Arctic Engineering*, New Orleans, LA, V. II, pp. 98-105.
- Shih, H.H., 1986. Design of Bubble Water Level Gauges for Dynamic Environment. *Proc. 9th Ann. Energy-Sources Technology Conference*, New Orleans, LA, pp. 411-418.
- Shih, H.H. and L. Baer, 1991. Some Errors in Tide Measurement Caused by Dynamic Environment. *Tidal Hydrodynamics*, B.B. Parker (Ed.), John Wiley & Sons, Inc., pp. 641-671.
- Smith, J.T., 1981. A History of Flying and Photography in the Photogrammetry Division of the National Ocean Survey, 1919-79. US Department of Commerce, Washington, D.C., 99.
- Schwarz, K.P, M. A. Chapman, M. W. Cannon, and P. Gong, 1993. An integrated INS/GPS approach to the georeferencing of remotely sensed data. *Photogrammetric engineering and remote sensing*, 59(11), 1667-1674.
- Stockdon, H.F., A.H. Sallenger, J.H. List, and R.A. Holman, 2002. Estimation of shoreline position and change using airborne topographic Lidar Data. *Journal of Coastal Research*, 18, 502-513.
- Thieler, E.R., E.A. Himmelstoss, J.L. Zichichi, and A. Ergul, 2009. Digital Shoreline Analysis System (DSAS) version 4.0- An ArcGIS extension for calculating shoreline change, U.S. Geological Survey Open-File Report 2008-1278.
- Vaughn, C.R., J.L. Bufton, W.B. Krabill, and D. Rabine, 1996. Georeferencing of airborne laser altimeter measurements. *International Journal of Remote Sensing*, 17(11), 2185-2200.
- Wainwright, D.B., 1922. Plane Table Mapping. Department of Commerce, U.S. Coast and Geodetic Survey, 97p.

- White, S.A., C.E. Parrish, B.R. Calder, S. Pe'eri and Y. Rzhanov, 2011. Lidar-derived national shoreline: empirical and stochastic uncertainty analyses, *Journal of Coastal Research*, SI(62), 62-74.
- Woodlard, J.W., M. Aslaksen, J.LT Longenecker, and A. Ryerson, 2003. Shoreline mapping from airborne LiDAR in Shilshole Bay, Washington. *Proceedings of National Oceanic and Atmospheric Administration (NOAA) National Ocean Service (NOS), U.S. Hydrographic Conference*.
- World Resources Institute (WRI). 2000. World Resources: 2000-2001. Washington, DC: WRI.
- Wozencraft, J., and D. Millar, 2005. Airborne lidar and integrated technologies for coastal mapping and nautical charting. *Marine Technology Society Journal*. 39(3), 27-35.
- Xu D., H. Xue, D.A. Greenberg, 2006. A Numerical Study of the Circulation and Drifter Trajectories in Cobscook Bay. *Proceedings of the 9th International Conference on Estuarine and Coastal Modeling*, Charleston, South Carolina, pp. 176- 194.
- Yuan X.X., X.P. Zhang, 2008. Theoretical accuracy of direct georeferencing with position and orientation system in aerial photogrammetry. *The International Archives of the Photogrammetry, Remote Sensing and Spatial Sciences*, Beijing, 37(B1): 617-622.
- Zhang, X.P., and X.X. Yuan, 2008. Effects of Exterior Orientation Elements on Direct Georeferencing in POS-Supported Aerial Photogrammetry. *Proceedings of the 8th International Symposium on Spatial Accuracy Assessment in Natural Resources and Environmental Sciences*, Shanghai, June 25-27: 30-36.

APPENDIX: TIDE ANALYSIS REPORT FOR ME1001

Tide Analysis Report for ME1001

EASPORT, ME ref stn

measured tide levels

| Station | Date | Time | Pred 6 | Vrfy 6 |
|---------|----------|-------|--------|--------|
| 8410140 | 20110621 | 13:18 | 0.97 | 1.27 |
| 8410140 | 20110621 | 13:24 | 0.87 | 1.14 |
| 8410140 | 20110621 | 14:06 | 0.88 | 1.08 |
| 8410140 | 20110621 | 14:18 | 1.11 | 1.31 |

*high/low*s

| | | | | |
|---------|----------|-------|-------|----|
| 8410140 | 20110621 | 07:24 | 19.15 | HH |
| 8410140 | 20110621 | 13:48 | 0.93 | LL |
| 8410140 | 20110621 | 19:42 | 18.62 | HH |

datums (ft)

| | |
|----------------------|-------|
| Mean High Water | 23.59 |
| Mean Lower-Low Water | 4.80 |
| (diff betw MHW-MLLW) | 18.79 |

| <i>Station</i> | <i>Mean Range</i> | <i>Tolerance</i> |
|----------------|-------------------|---|
| EASTPORT | 18.35 | MLLW betw -1.835 ft (-0.56 m) and 1.835 ft (0.56 m) |
| CoffinsPt | 17.3 | MLLW betw -1.73 ft (-0.53 m) and 1.73 ft (0.53 m) |
| BirchIsle | 17.4 | MLLW betw -1.74 ft (-0.53 m) and 1.74 ft (0.53 m) |

Reference station:

EASTPORT, ME

Jun 21, 2011, 13:18 GMT

Actual tide level: 1.27 ft MLLW

| High/low times | WL (MLLW) |
|----------------|-----------|
| 07:24 GMT | 19.15 ft |
| 13:48 GMT | 0.93 ft |

Subordinate stations:Birch Islands

Reference station: Eastport, Corrections Applied:

Times: High +0 hr. 59 min., Low +1 hr. 13 min., **Heights:** High *0.94, Low *0.75

| High/low times | WL (MLLW) | Duration | Time to H/L | Range |
|----------------|-----------|----------|-------------|----------|
| 08:23 GMT | 18.0 ft | 6:38 | 1:43 | 17.30 ft |
| 15:01 GMT | 0.70 ft | | | |

Calculated tide level: 3.6 ft (MLLW)

Coffins Point

Reference station: Eastport, Corrections Applied:

Times: High +0 hr. 31 min., Low +0 hr. 33 min., **Heights:** High *0.94, Low *0.77

| High/low times | WL (MLLW) | Duration | Time to H/L | Range |
|----------------|-----------|----------|-------------|-------|
| 07:55 GMT | 18.0 ft | 6:26 | 1:03 | 17.28 |
| 14:21 GMT | 0.72 ft | | | |

Calculated tide level: 1.92 ft (MLLW)

Reference station:

EASTPORT, ME

Jun 21, 2011, 13:24 GMT

Actual tide level: 1.14 ft MLLW

| High/low times | WL (MLLW) |
|----------------|-----------|
| 07:24 GMT | 19.15 ft |
| 13:48 GMT | 0.93 ft |

Subordinate stations:Birch Islands

Reference station: Eastport, Corrections Applied:

Times: High +0 hr. 59 min., Low +1 hr. 13 min., **Heights:** High *0.94, Low *0.75

| High/low times | WL (MLLW) | Duration | Time to H/L | Range |
|----------------|-----------|----------|-------------|----------|
| 08:23 GMT | 18.0 ft | 6:38 | 1:37 | 17.30 ft |
| 15:01 GMT | 0.70 ft | | | |

Calculated tide level: 2.90 ft (MLLW)

Coffins Point

Reference station: Eastport, Corrections Applied:

Times: High +0 hr. 31 min., Low +0 hr. 33 min., **Heights:** High *0.94, Low *0.77

| High/low times | WL (MLLW) | Duration | Time to H/L | Range |
|----------------|-----------|----------|-------------|-------|
| 07:55 GMT | 18.0 ft | 6:26 | 0:57 | 17.28 |
| 14:21 GMT | 0.72 ft | | | |

Calculated tide level: 1.90 ft (MLLW)

Reference station:

EASTPORT, ME

Jun 21, 2011, 14:06 GMT

Actual tide level: 1.08 ft MLLW

| High/low times | WL (MLLW) |
|----------------|-----------|
| 13:48 GMT | 0.93 ft |
| 19:42 GMT | 18.62 ft |

Subordinate stations:Birch Islands

Reference station: Eastport, Corrections Applied:

Times: High +0 hr. 59 min., Low +1 hr. 13 min., **Heights:** High *0.94, Low *0.75

| High/low times | WL (MLLW) | Duration | Time to H/L | Range |
|----------------|-----------|----------|-------------|----------|
| 14:47 GMT | 0.87 ft | 6:08 | 0:41 | 13.09 ft |
| 20:55 GMT | 13.97 ft | | | |

Calculated tide level: 1.17 ft (MLLW)

Coffins Point

Reference station: Eastport, Corrections Applied:

Times: High +0 hr. 31 min., Low +0 hr. 33 min., **Heights:** High *0.94, Low *0.77

| High/low times | WL (MLLW) | Duration | Time to H/L | Range |
|----------------|-----------|----------|-------------|----------|
| 14:19 GMT | 0.87 ft | 5:56 | 0:13 | 13:46 ft |
| 20:15 GMT | 14.34 ft | | | |

Calculated tide level: 0.87 ft (MLLW)

Reference station:

EASTPORT, ME

Jun 21, 2011, 14:18 GMT

Actual tide level: 1.31 ft MLLW

| High/low times | WL (MLLW) |
|----------------|-----------|
| 13:48 GMT | 0.93 ft |
| 19:42 GMT | 18.62 ft |

Subordinate stations:Birch Islands

Reference station: Eastport, Corrections Applied:

Times: High +0 hr. 59 min., Low +1 hr. 13 min., **Heights:** High *0.94, Low *0.75

| High/low times | WL (MLLW) | Duration | Time to H/L | Range |
|----------------|-----------|----------|-------------|----------|
| 14:47 GMT | 0.87 ft | 6:08 | 0:29 | 13.09 ft |
| 20:55 GMT | 13.97 ft | | | |

Calculated tide level: 0.97 ft (MLLW)

Coffins Point

Reference station: Eastport, Corrections Applied:

Times: High +0 hr. 31 min., Low +0 hr. 33 min., **Heights:** High *0.94, Low *0.77

| High/low times | WL (MLLW) | Duration | Time to H/L | Range |
|----------------|-----------|----------|-------------|----------|
| 14:19 GMT | 0.87 ft | 5:56 | 0:01 | 13:46 ft |
| 20:15 GMT | 14.34 ft | | | |

Calculated tide level: 0.87 ft (MLLW)